MODELING SOURCE ROCK MICRO-STRUCTURAL AND ELASTIC CHANGES DURING THERMAL MATURATION

A DISSERTATION
SUBMITTED TO THE DEPARTMENT OF GEOPHYSICS
AND THE COMMITTEE ON GRADUATE STUDIES
OF STANFORD UNIVERSITY
IN PARTIAL FULFILLMENT OF THE REQUIREMENTS
FOR THE DEGREE OF
DOCTOR OF PHILOSOPHY

Yunfei Yang

February 2019

I certify that I have read this dissertation and that, in my opinion, it is fully adequate in scope and quality as a dissertation for the degree of Doctor of Philosophy.

Gerald Mavko, Primary Adviser

I certify that I have read this dissertation and that, in my opinion, it is fully adequate in scope and quality as a dissertation for the degree of Doctor of Philosophy.

Eric Dunham

I certify that I have read this dissertation and that, in my opinion, it is fully adequate in scope and quality as a dissertation for the degree of Doctor of Philosophy.

Tapan Mukerji

Approved for the Stanford University Committee on Graduate Studies.

Patricia J. Gumport, Vice Provost for Graduate Education

This signature page was generated electronically upon submission of this dissertation in electronic format. An original signed hard copy of the signature page is on file in University Archives.

Abstract

I first present a mathematical model that predicts the microcrack growth and pore pressure change during the organic-rich source rock thermal maturation. This model is primarily based on elasticity and the principle of linear elastic fracture mechanics. By running the simulation under laboratory conditions, I obtain similar fracture surface areas to those measured by Kobchenko et al. (2014) [42]. Secondary porosity generated by crack opening is significant under laboratory conditions: the induced crack volume can accommodate several hundred times the initial pore volume. In contrast, under geological conditions, no significant secondary porosity is generated through crack opening. If the kerogen-to-hydrocarbon density ratio is sufficiently high, overpressure can be built up more quickly, and microcracks can propagate at earlier maturation stage. However, the extent of propagation and resulting apertures are much smaller than those generated under laboratory settings because of the overburden effect.

Following the single crack model, I then introduce an improved rock physics modeling workflow using the effective medium theory to quantify the source rock elastic property evolution as the rock matures. The source rock system is divided into an inorganic background matrix containing minerals and water- or air-filled pores, and organics-filled inclusions. The differential effective medium algorithm is used twice in building the source rock system: it is first used to build an effective medium for the organic part, and then is used to build an effective medium for the source rock system. I make use of the experimental data, in particular the data of yields collected from

the hydrous pyrolysis experiments to constrain the inputs to the rock physics models.

The modeling results show that the thermal maturation first results in the reduction of the P- and S-wave moduli in the organic mixture; the most pronounced reduction occurs in the oil window corresponding to a vitrinite reflectance range of 0.6-0.8%. The sensitivity analysis further shows that good measurements of the elastic properties of the solid organic components (kerogen and bitumen) are more critical than those of the fluids for achieving accurate elastic constant predictions for the organic mixture. From the source rock system perspective, the thermal maturation results in enhanced anisotropy and reduced elastic stiffness. The organic inclusions with lower aspect ratios result in more significant reduction in the elastic stiffness, and more significant increase in the anisotropy. The elastic stiffness components of the source rock that have either the particle motion or the associated wave propagation direction parallel to the axis of the rotational symmetry of the inclusions are more sensitive to the elastic property change within the organic part.

Last but not the least, I introduce an improved deep learning based framework to classify seismic facies from three-dimensional (3D) seismic volumes. By fine-tuning the convolutional neural network (CNN) hyper-parameters based off the "MalenoV" repository [34], I obtain a better architecture named the modified LeNet-5. I also implement a "sparse sampling" scheme to pre-process the input data, which allows the input data size to be much smaller while maintaining a relatively large receptive field. The improved 3D CNN framework significantly improves the training and validation accuracy in the early training stage. Specifically, the combined use of the modified LeNet-5 and the sparse sampling scheme attains the best metrics in terms of the test accuracy. I conclude that the 3D CNN framework is very promising in making geologically reasonable and consistent predictions for seismic facies based on 3D seismic volumes.

Acknowledgments

First, I would like to thank my primary PhD advisor, Prof. Gary Mavko. Till today, I still feel very fortunate that he took me into the Stanford Rock Physics group even though I knew little about rock physics or geophysics. It was Gary's strong belief in my abilities, his patience and encouragement that have propelled me to overcome difficulties over the past few years. Gary is my academic advisor, but also my lifelong mentor. Second, I would like to thank my co-advisor, Prof. Tapan Mukerji. Tapan's broad expertise in rock physics, basin modeling, statistics and machine learning enabled me to find directions no matter what problems I encountered in my research. He always has insightful ideas, or sees the bigger picture in any small pieces of research I did. I am also grateful for the internship opportunity that he brought to his students: I learned a ton from my two summers at Halliburton. I would also like to thank Dr. Jack Dvorkin, who gave me many practical guidance in rock physics modeling, and introduced me to several international opportunities to get to know the rock physics community worldwide. It was indeed my privilege to work with the best rock physicists in the world at Stanford over the past few years.

I thank Prof. Eric Dunham, Prof. Amos Nur, Prof. Mark Zoback, Dr. Bob Clapp and Dr. Shuki Ronen for providing extra guidance for my research over the past few years. I thank Prof. Tiziana Vanorio, Dr. Stephanie Vialle, Dr. Tony Clark, Shaoyu Lu, Yu Xia, Yi Shen and Lucile Bruhat, who helped me tremendously in the early

days when I transitioned from mechanical engineering to geophysics. I thank my office-mates, Chao Liang, Abdulla Kerimov, Priyanka Dutta, Shaochuan Xu, Jeremy Mauer and Meredith Goebel, who have made my days (and nights) at Mitchell fun and less lonely. I thank the department administers and my colleagues and friends from the SRB family, who are always there when I need help and support: Jared, Nancy, Rachael, Corey, Dario, Adam, Yuki, Chisato, Nishank, Sabrina, Humberto, Abrar, Salma, Natt, Vishal, Uri, Osama, Omar, Juan-Pablo, Monirah, Rayan, Obi, Jim, Zhishuai, Fabian, Helene and Bin. I also thank my friends from Geophysics, GES, ERE and CEE for the fun times together: Lei, Huiying, Tianze, Dongzhuo, Yixiao, Zhipeng, Yihe, Krongrath, Dulcie, Yunyue, Hui, Ettore, Guillaume, Fantine, Kevin, Xiaodong, Gader, Fatimah, Robert, Fatemah, Yujie, Ying-Qi, Beibei, Peipei, Qing, Bo, Mengyao, Wenhao, Jie, Fan, Chuan, Wenyue, Guang, Larry, Yuran, Haoli, Yuchi, Yifan, Yimin, Jingfan, Renfeng, Batool, Michael and Yaxin.

I should not forget to thank my friends from my Master's time: Holly He, Yunhan Chen, Diana Tang, Yushi Yang, Ming Pan, Lin Fan, Yibo Cai, and many more. I should also thank my badminton friends: Chen Guo, Yixin Tang, Daniel Liu, Xinyu Shen, Bowen Ling, Kang Liu, Shanshan Chen, Junfeng He, Jim Zhu, Yibo Cai, Bing Wu, Chaoming Jian, Xukai Shen, and many more. Thank you for the good times; I cherish the friendship with each one of you.

I deeply thank my boyfriend, Wei Chu, for his love, support and many constructive inputs to my research. He gave me the peace of mind that allows me to focus on my study. Finally, I would like to thank my parents, Zhengyang Tuo and Jinglu Yang, for their unwavering love and support, and for bringing me up into the person I am today.

Contents

List of Tables

List of Figures

Chapter 1

Introduction

1.1 Source rocks and the kerogen

Petroleum source rocks are defined as the organic-rich rock units which have or had the capability of generating and expel hydrocarbons at appropriate maturity levels, allowing a commercial hydrocarbon accumulation [40]. Generally speaking, a naturally deposited source rock must undergo diagenesis before generating significant amount of hydrocarbons. Diagenesis refers to the shallow burial stage with near-surface temperatures up to about 60 °C. Organic matter is degraded; methane, carbon dioxide, and water are produced. Kerogen, a precursor to petroleum, and bitumen, are also formed. Kerogen is a solid organic compound mixture. It differs from bitumen by the fact that it is insoluble in organic solvents. The kerogen is typically classified by its sedimentation environment and sources of organic compounds: Type I (algal derived), Type II (terrestrial and marine derived), Type IIS (sulfur rich), Type III (terrestrial derived), and Type IV (inert, non-source) [76]. The diagenesis is followed by the catagenesis, during which hydrocarbons are generated from the kerogen. The catagenesis usually occurs at a medium burial stage corresponding to a temperature range between 60 and 175 °C [76]. The maturity level of a source rock reflects

the stage at which the kerogen converts into hydrocarbons. A source rock can be immature, mature, or over-mature depending on whether or not the majority of the kerogen-to-hydrocarbon conversion has occurred. Geochemists often use three metrics to determine the quantity, quality, and thermal maturity of source rocks: vitrinite reflectance, total organic carbon (TOC), and data from Rock-Eval pyrolysis.

1.1.1 Vitrinite reflectance

Vitrinite reflectance is a measure of the percentage of incident light reflected from the surface of vitrinite particles in a rock sample. It is usually abbreviated as Ro or %Ro, which reflects the fact that it is reported in percentage. The reported vitrinite reflectance is usually a mean value based on all the vitrinite particles measured in an individual sample. Vitrinite reflectance reflects the source rock maturity level. Roughly speaking, an Ro value between 0.2% and 0.6% corresponds to an immature source rock; 0.6-1.35 %Ro covers the mature range; a value greater than 1.35 %Ro indicates an over-mature source rock [63]. The vitrinite reflectance can be calculated by invoking vitrinite reflectance kinetics models. Among many such models, Easy %Ro proposed by [72] is most commonly used, and will be discussed in more details in Chapter 3.

1.1.2 TOC

The total organic carbon, or abbreviated as TOC, refers to the percentage of organic carbon by weight present in a piece of source rock. The TOC content consists of three components: the carbon in extractable organic matter (EOM carbon), convertible carbon, and a residual carbon fraction. The EOM carbon is composed of the carbon contained in the hydrocarbons that are already formed [37]. The EOM carbon is generally a very small fraction of the TOC. In a typical shale or carbonate sample,

the EOM carbon fraction is less than 1% of the TOC itself. The second component of the TOC content is the convertible carbon contained in the kerogen. The convertible carbon represents the remaining potential of the rock to generate hydrocarbons. The residual carbon component is also part of the kerogen and represents a form of organic carbon that has no potential to generate hydrocarbons due to its chemical structure and composition. In the unconventional exploration and production, the TOC of a source rock is generally treated as the kerogen content.

1.1.3 Rock-Eval pyrolysis

Pyrolysis is the decomposition of organic matter by heating in the absence of oxygen. Organic geochemists perform pyrolysis to measure the richness and maturity of potential source rocks. The most widely used pyrolysis technique is the Rock-Eval. Rock-Eval is a programmed pyrolysis specified as follows: a sample is placed in a vessel and is progressively heated to 550 °C under an inert atmosphere (helium). The oven is kept isothermal at 300 °C for three minutes, while the flame ionization detector (FID) measures the released hydrocarbons reported as the S1 peak. The temperature is then increased from 300 °C to 550 °C at 25 °C/min, during which the volatilization of heavy hydrocarbon compounds and the cracking of nonvolatile organic matter occur. The FID measures the released hydrocarbons, and records the S2 peak. The temperature at which S2 reaches its maximum depends on the nature and maturity of the kerogen, and is called the Tmax. Finally, the CO_2 generated from kerogen cracking is recorded as the S3 peak by a thermal conductivity detector during the cooling of the pyrolysis oven [76, 64]. In summary, the four basic parameters obtained from the Rock-Eval are as follows:

- S1: Amount of hydrocarbons thermally extracted at 300 °C;
- S2: Amount of hydrocarbons produced from pyrolysis up to 550 °C;

- S3: Amount of CO_2 released from kerogen cracking at higher temperatures;
- Tmax: Temperature at the S2 peak.

The type and maturity of the organic matter in the source rocks can be characterized from Rock-Eval pyrolysis data using the following parameters:

- HI: Hydrogen index (HI = [100 x S2]/TOC). HI is a parameter that correlates with the atomic hydrogen/carbon ratio. HI typically ranges from 100 to 600. Under the same maturity level, a good quality source rock (e.g. source rocks with type I kerogen) has higher HI (e.g. HI > 700). HI also serves as a maturity indicator, as it decreases as the source rock matures.
- OI: Oxygen index (OI = [100 x S3]/TOC). OI is a parameter that correlates with the oxygen/carbon ratio. OI typically ranges from 0 to 150.
- PI: Production index (PI = S1/[S1 + S2]). PI is used to characterize the evolution level of the organic matter.

The HI and HI indices collected from Rock-Eval can be used to calculate the hydrogen-to-carbon (H/C) and oxygen-to-carbon (O/C) ratios. Different kerogen types fall into different groups when plotted on the van Krevelen diagram, as shown in Figure 1.1. We also observe that both the H/C and O/C reduce as the source rock matures.

1.1.4 Hydrous pyrolysis

Among various types of pyrolysis experiments, hydrous pyrolysis is known to produce expelled hydrocarbons resembling the naturally occurring crude oil ([48][49]). With proper experimental setups, physical properties of generated hydrocarbons, such as the gas-to-oil ratio (GOR) and API density, can be measured during the hydrous pyrolysis process ([50][25][70]). The knowledge of the compositional and physical properties of

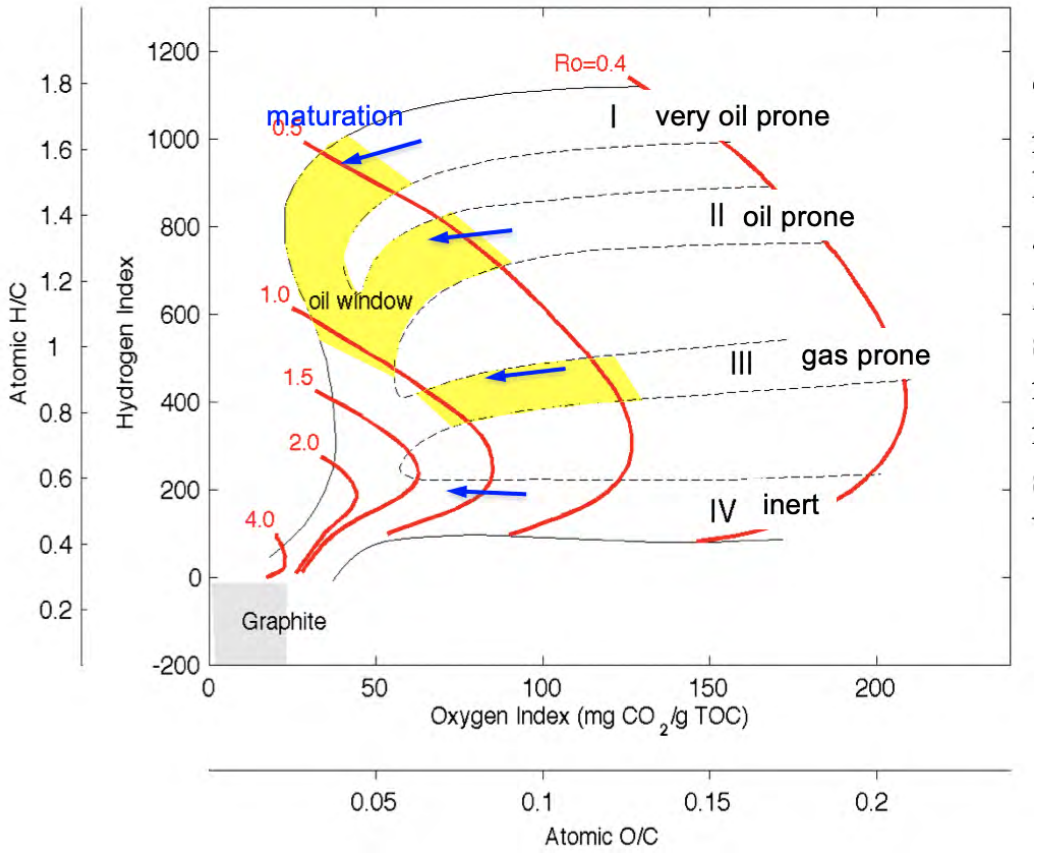

Figure 1.1: van Krevelen diagram and the thermal maturation pathways.

the generated hydrocarbons allows us to connect geochemistry with geophysics via rock physics modeling: the change in elastic properties of source rocks as a consequence of thermal maturation can be reflected and interpreted from geophysical measurements and proper rock physics modeling.

1.1.5 Primary migration

Primary migration refers to the transport process by which the hydrocarbon that is generated from the kerogen emigrates from the source rock, and ultimately arrives at the carrier beds (Selley, 2014 [68]) . The mechanism of the primary migration remains an important question for petroleum geologists: after all, the source rock is almost impermeable. Selley (2014) [68] gave a comprehensive review of the proposed primary migration mechanisms by various authors. Theories were essentially based on different hypotheses of the solution nature (water, oil and/or gas). Berg and Gangi (1999) [11] argued that the primary migration through fractures is attractive because fractures have high permeability. Vernik (1994) [78] showed that subhorizontal microcracks are consequences of the hydrocarbon generation, and thus contribute to the creation of migration pathways within the source rock. It can be concluded that primary migration through cracks and fractures in the source rock, among other possible migration hypotheses, is a possible mechanism which ties to the overpressure generated from hydrocarbons.

1.2 Governing equations, elasticity and anisotropy

1.2.1 Wave equation and constitutive equation

The seismic waves propagating in the subsurface as well as ultrasonic waves propagating in rock samples in the laboratory are both mechanical waves. The wave equation is

derived from the conservation of linear momentum. The balance of linear momentum in the i-th direction is given by

$$\rho \frac{\partial^2 u_i}{\partial t^2} - \frac{\partial \sigma_{ij}}{\partial x_j} = f_i, \tag{1.1}$$

where ρ is the density of the medium, t is the time, u_i is the displacement in the i-th direction, σ_{ij} is the stress tensor, x_j is the spatial position in the j-th direction in the Cartesian coordinates, and f_i is the body force in the i-th direction expressed in the unit of force per unit volume. The indicial (Einstein's) notation is implicitly used here, where the repeated index suggests a summation over all dimensions.

Eqn.(1.1) is usually used in conjunction with a constitutive equation to derive an expression for the displacement u_i. The constitutive equation for linearly elastic and homogeneous media is given by

$$\sigma_{ij} = c_{ijkl} e_{kl}, \tag{1.2}$$

where c_{ijkl} is the linear elastic stiffness tensor of the medium, and e_{kl} is the strain tensor, which is defined as

$$e_{kl} = \frac{1}{2}\left(\frac{\partial u_k}{\partial x_l} + \frac{\partial u_l}{\partial x_k}\right). \tag{1.3}$$

Note that the strain tensor is a second-rank symmetric tensor by construction ($e_{kl} = e_{lk}$); the stress tensor is also symmetric due to the force balance ($\sigma_{ij} = \sigma_{ji}$). Therefore, the elastic stiffness tensor c_{ijkl} has a minor symmetry where $c_{ijkl} = c_{jikl} = c_{jilk}$. Combining Eqns.(1.1)(1.2)(1.3), we can derive the general wave equation expressed in terms of the displacement vector $\mathbf{u}$

$$\rho \frac{\partial^2 u_i}{\partial t^2} - c_{ijkl} \frac{\partial^2 u_k}{\partial x_j \partial x_l} = f_i. \tag{1.4}$$

1.2.2 Christoffel equation and plane waves

In the absence of body force f_i, Eqn.(1.4) becomes

$$\rho\frac{\partial^2 u_i}{\partial t^2} - c_{ijkl}\frac{\partial^2 u_k}{\partial x_j \partial x_l} = 0. \tag{1.5}$$

To solve this homogeneous wave equation, we can use a trial solution in the form of plane waves

$$u_k = U_k \exp\left(i\omega(n_j x_j/V - t)\right) \tag{1.6}$$

where U_k is the k-th component of the polarization vector $\mathbf{U}$, ω is the angular frequency, V is the phase velocity of the wave modes, and n_j is the j-th component of the unit vector orthogonal to the plane wave front (the wave front satisfies $n_j x_j - Vt = const$) [77]. Substituting Eqn.(1.6) into Eqn.(1.5), we obtain the Christoffel equation for the phase velocity V and polarization vector $\mathbf{U}$:

$$\begin{bmatrix} G_{11} - \rho V^2 & G_{12} & G_{13} \\ G_{21} & G_{22} - \rho V^2 & G_{23} \\ G_{31} & G_{32} & G_{33} - \rho V^2 \end{bmatrix} \begin{bmatrix} U_1 \\ U_2 \\ U_3 \end{bmatrix} = 0 \tag{1.7}$$

where G_{ik} is the Christoffel matrix the given by

$$G_{ik} = c_{ijkl} n_j n_l. \tag{1.8}$$

Eqn.(1.7) can also be rewritten as

$$[G_{ik} - \rho V^2 \delta_{ik}]U_k = 0 \tag{1.9}$$

where δ_{ik} is the Kronecker delta. To produce non-trivial solutions for $\mathbf{U}$, we impose

$$\det[G_{ik} - \rho V^2 \delta_{ik}] = 0. \tag{1.10}$$

It can be shown that G_{ik} is symmetric because of the symmetry of the stiffness tensor, and that G_{ik} is positive definite [57]. Therefore, the solution to Eqn.(1.10) gives three real and positive phase velocities Vs corresponding to three wave modes. The fastest one corresponds to the P-wave, and the two slower ones correspond to the two S-waves. In other words, an anisotropic medium splits the shear wave into two modes with different velocities and polarization. The isotropic medium is a degenerate case of the anisotropic medium, where the two S-wave velocities always coincide.

1.2.3 The Voigt notation and elastic stiffness tensor

The Voigt notation provides a convenient way to rewrite the fourth-rank tensor in a matrix form. Specifically, it groups the four free indices $ijkl$ into two pairs, (i, j) and (k, l), and maps (i, j) into index I, and (k, l) into index J in the matrix C_{IJ}. The mapping follows the rules
$(1, 1) \to 1; (2, 2) \to 2; (3, 3) \to 3; (2, 3)(3, 2) \to 4; (1, 3)(3, 1) \to 5; (1, 2)(2, 1) \to 6.$

For instance, the fourth-rank elastic stiffness tensor for isotropic media is given by

$$c_{ijkl} = \lambda \delta_{ij} \delta_{kl} + \mu(\delta_{ik}\delta_{jl} + \delta_{il}\delta_{jk}), \tag{1.11}$$

where λ and μ are the Lamé constants. In the Voigt notation, Eqn.(1.11) is written as

$$\mathbf{C} = \begin{bmatrix} \lambda+2\mu & \lambda & \lambda & 0 & 0 & 0 \\ \lambda & \lambda+2\mu & \lambda & 0 & 0 & 0 \\ \lambda & \lambda & \lambda+2\mu & 0 & 0 & 0 \\ 0 & 0 & 0 & \mu & 0 & 0 \\ 0 & 0 & 0 & 0 & \mu & 0 \\ 0 & 0 & 0 & 0 & 0 & \mu \end{bmatrix}. \tag{1.12}$$

Note that two independent elastic constants (e.g. λ and μ) can fully characterize the elastic stiffness tensor for isotropic media. The vertical transversely symmetric (VTI) medium refers to the case where the medium preserves rotational symmetry along the vertical, or the 3-direction. The VTI medium can be characterized by five independent elastic constants, such as c_{11}, c_{33}, c_{55}, c_{66} and c_{13}. In the Voigt notation, the elastic stiffness tensor for VTI media is written as

$$\mathbf{C} = \begin{bmatrix} c_{11} & c_{11}-2c_{66} & c_{13} & 0 & 0 & 0 \\ c_{11}-2c_{66} & c_{11} & c_{13} & 0 & 0 & 0 \\ c_{13} & c_{13} & c_{33} & 0 & 0 & 0 \\ 0 & 0 & 0 & c_{55} & 0 & 0 \\ 0 & 0 & 0 & 0 & c_{55} & 0 \\ 0 & 0 & 0 & 0 & 0 & c_{66} \end{bmatrix} \tag{1.13}$$

where we have used the facts that $c_{11} = c_{22}$, $c_{44} = c_{55}$, and $c_{12} = c_{11} - 2c_{66}$.

1.2.4 Wave propagation in VTI media

It follows that the entries in the Christoffel matrix for VTI media are given by [77]

$$\begin{aligned} G_{11} &= c_{11}n_1^2 + c_{66}n_2^2 + c_{55}n_3^2, \\ G_{22} &= c_{66}n_1^2 + c_{11}n_2^2 + c_{55}n_3^2, \\ G_{33} &= c_{55}(n_1^2 + n_2^2) + c_{33}n_3^2, \\ G_{12} &= (c_{11} - c_{66})n_1n_2, \\ G_{13} &= (c_{13} + c_{55})n_1n_3, \\ G_{12} &= (c_{13} + c_{55})n_2n_3. \end{aligned} \tag{1.14}$$

Since any planes containing the symmetry axis (3-axis) are equivalent for VTI media, we can just study the wave propagation in a single vertical plane. For instance, by choosing the $[x_1, x_3]$-plane ($n_2 = 0$), the Christoffel equation becomes

$$\begin{bmatrix} c_{11}n_1^2 + c_{55}n_3^2 - \rho V^2 & 0 & (c_{13} + c_{55})n_1n_3 \\ 0 & c_{66}n_1^2 + c_{55}n_3^2 - \rho V^2 & 0 \\ (c_{13} + c_{55})n_1n_3 & 0 & c_{55}n_1^2 + c_{33}n_3^2 - \rho V^2 \end{bmatrix} \begin{bmatrix} U_1 \\ U_2 \\ U_3 \end{bmatrix} = 0. \tag{1.15}$$

Note that Eqn.(1.15) can be split into two independent equations for the pure transverse motion ($U_1 = U_3 = 0$) and in-plane motion ($U_2 = 0$). Expressing the unit vector $\mathbf{n}$ in terms of the angle θ with respect to the 3-direction, we have

$$\begin{aligned} n_1 &= \sin\theta \\ n_3 &= \cos\theta. \end{aligned} \tag{1.16}$$

From the transverse motion ($U_1 = U_3 = 0$), we can derive the phase velocity of the SH-wave to be

$$V_{SH}(\theta) = \sqrt{\frac{c_{66}\sin^2\theta + c_{55}\cos^2\theta}{\rho}}. \tag{1.17}$$

For vertically propagating waves ($\theta = 0$), $V_{SH}(\theta = 0) = \sqrt{c_{55}/\rho}$. For horizontally propagating waves ($\theta = 90°$), $V_{SH}(\theta = 90°) = \sqrt{c_{66}/\rho}$. Likewise, from the in-plane motion ($U_2 = 0$), we can derive the other two phase velocities, representing the P- and SV-waves:

$$\begin{aligned} V_P(\theta = 0) &= \sqrt{\frac{c_{33}}{\rho}}, \\ V_{SV}(\theta = 0) &= \sqrt{\frac{c_{55}}{\rho}}, \end{aligned} \tag{1.18}$$

and

$$\begin{aligned} V_P(\theta = 90°) &= \sqrt{\frac{c_{11}}{\rho}}, \\ V_{SV}(\theta = 90°) &= \sqrt{\frac{c_{55}}{\rho}}. \end{aligned} \tag{1.19}$$

We can observe that in the VTI medium, the SH- and SV-modes propagate at the same speed for vertically propagating waves ($\theta = 0$). For horizontally propagating waves ($\theta = 90°$), the SH- and SV-modes propagate in different speeds, resulting in shear-wave splitting. The SV-wave travels at the same speed at both vertical and horizontal directions, but not necessarily at oblique directions, where $0 < \theta < 90°$. Finally, the P-wave travels at different speeds along the vertical and horizontal directions.

1.2.5 Thomsen anisotropy parameters

We've shown that the VTI elastic stiffness tensor $\mathbf{C}$ can be fully characterized by five elastic parameters. Thomsen (1986) [73] introduced the reparametrization for the

VTI structure, so that $\mathbf{C}$ can be characterized by vertical velocities V_{P0}, V_{S0} of P- and S-wave, respectively, and three dimensionless anisotropy parameters denoted as ϵ, δ and γ. Formally, these five quantities are given by

$$\begin{aligned} V_{P0} &= \sqrt{\frac{c_{33}}{\rho}}, \\ V_{S0} &= \sqrt{\frac{c_{55}}{\rho}}, \\ \epsilon &= \frac{c_{11} - c_{33}}{2c_{33}}, \\ \delta &= \frac{(c_{13} + c_{55})^2 - (c_{33} - c_{55})^2}{2c_{33}(c_{33} - c_{55})}, \\ \gamma &= \frac{c_{66} - c_{55}}{2c_{55}}. \end{aligned} \tag{1.20}$$

The ϵ, δ and γ are also called the Thomsen parameters. In particular, ϵ denotes the P-wave anisotropy, γ denotes the SH-wave anisotropy, and δ determines the second derivative of the P-wave phase-velocity function at vertical incidence. δ is positive if the P-wave phase velocity increases away from the vertical direction [77].

1.3 Literature review

1.3.1 Experimental evidence of microcracks in source rocks

With the help of scanning electron microscopy (SEM), geoscientists have found microcracks resulting from hydrocarbon generation; these are thought to be instrumental to fluid transport processes [14, 11, 46, 22, 83]. Ougier-Simonin et al. (2016) [60] provided a comprehensive review of possible mechanisms in shale that can result in microfractures and microcracks. Lash and Engelder (2005) [46] showed SEM images (Figure 1.2) of the Upper Devonian Dunkirk Shale of New York, where sub-horizontal microcracks are clearly visible. The length and aperture of the cracks vary; most

are bitumen-filled. More importantly, the authors identified cracks that originated within the kerogen, providing evidence that overpressure associated with kerogen maturation can cause the formation of microcracks. Kobchenko et al. (2014) [42] applied time-resolved X-ray tomography imaging on a shale sample undergoing heating process, and observed the formation of microcracks associated with kerogen decomposition (Figure 1.3). Vernik (1994) [78] observed a stronger sensitivity of ultrasonic P-wave velocity to confining pressure for more mature organic-rich shale samples, and concluded that the bedding-parallel microcracks that prevail in those samples result from hydrocarbon generation. Recently, Allan et al. (2016) [4] conducted pyrolysis experiments on different organic-rich shale samples under various confining stresses. They observed variation in the acoustic velocity and anisotropy on selected samples after pyrolysis. These experimental observations further indicate the creation of microcracks during source rock thermal maturation, mostly likely caused by the overpressure generated by hydrocarbon expulsion.

1.3.2 Mechanical models of the source rock system

Earlier studies have attempted to model hydrocarbon generation-related crack initiation and propagation at microscopic levels using various mechanical models and fracture initiation criteria. Özkaya (1988) [61] assumed a two-dimensional (2D) model, and discussed favorable conditions for vertical and horizontal crack initiation caused by overpressure associated with kerogen-to-oil conversion, concluding that the far-field stress state, elastic properties, kerogen morphology, and permeability of the rock matrix all play important roles in the creation of hydrocarbon-induced cracks. Luo and Vasseur (1996) [53] calculated the overpressure induced by the oil and gas generation using a two-phase hydrodynamic model; they concluded that oil generation does not contribute to the overpressure significantly except when the total organic matter is high (5 wt.% to 10 wt.%), and that gas generation can cause significant overpressure

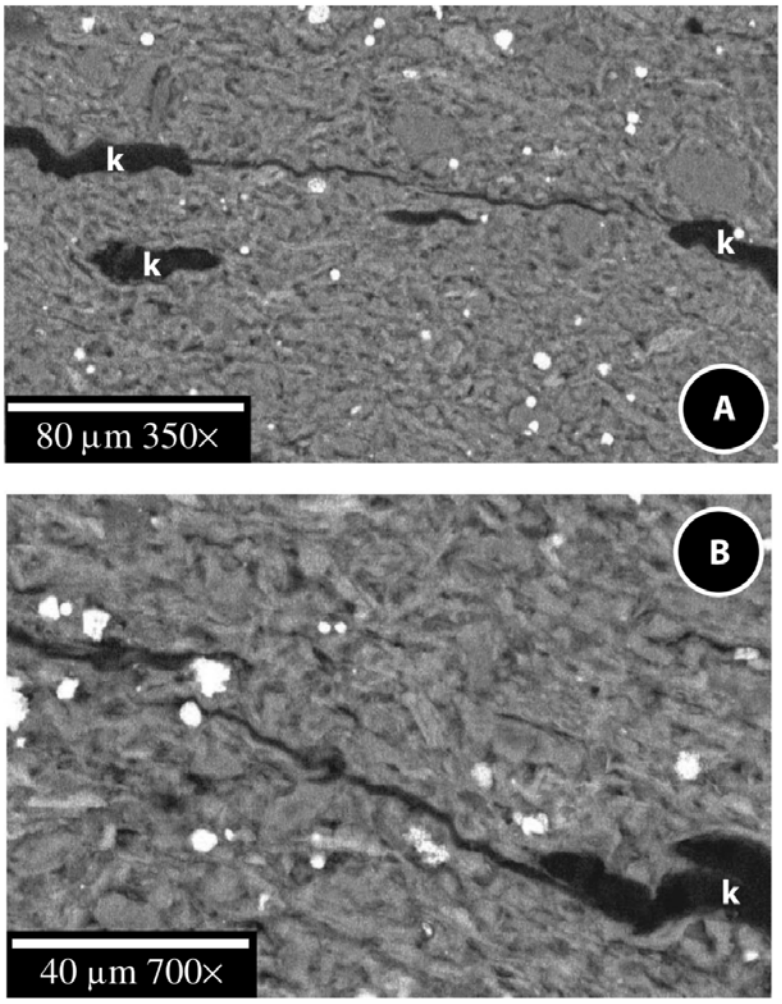

Figure 1.2: SEM images showing microcracks that have originated within (or along the edges of) kerogen (k) particles [46].

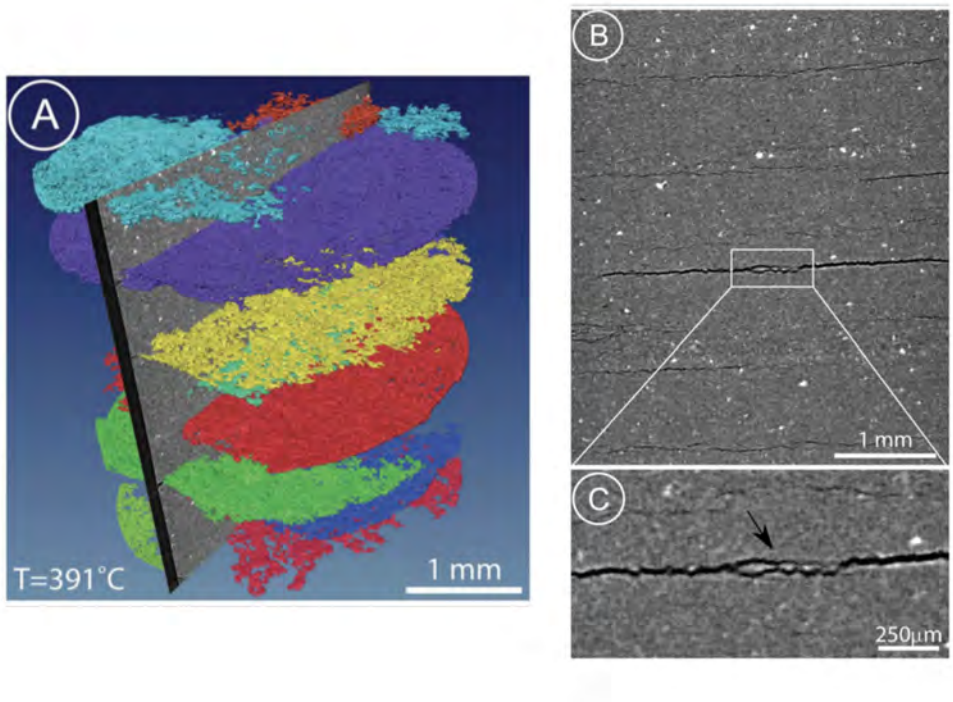

Figure 1.3: Tomography images of the shale sample at 391C, corresponding to the moment of maximum crack opening. (a) 3D rendering of final crack network. Each color defines an independent crack. (b) 2D slice showing (dark color) elongated cracks that developed parallel to the bedding. (c) Details of (b) showing a crack developed around a pyrite grain (arrow). Redrawn after [42].

that usually takes place during the secondary cracking of oil. Coussy et al. (1998) [21] assumed a 2D kerogen-pore-matrix system to calculate the amount of overpressure based on linear elasticity, and modeled microcrack initiation in the matrix using the Griffith tensile-strength criterion. They found that if the variation in the far-field stress is neglected during the overpressure buildup, the resulting excess pore pressure can initiate microcracks. Assuming a three-dimensional (3D), hydrocarbon-filled penny-shaped crack embedded in a kerogen-shale solid, Jin et al. (2010) [38] and Fan et al. (2010, 2012) [28, 29] estimated crack growth using subcritical fracture propagation criterion introduced by Atkinson (1984) [7] for both isotropic and VTI shale backgrounds.

1.3.3 Effective medium modeling for source rock systems

Rock physics modeling for source rocks has been a continuous effort. Nishizawa (1982) [59] and Hornby et al. (1992) [32] established theoretical frameworks for modeling VTI effective media using the differential effective medium (DEM) modeling. Carcione et al. (2011) [16] used Kuster and Toksöz model (Kuster and Toksöz, 1974 [44]) to model the oil-kerogen mixture, and used Backus averaging (Backus, 1962 [8]) and Gassmann equations (Ciz and Shapiro, 2007 [19]) to model the VTI source rock. Sayers (2013) [67] applied Sevostianov et al. (2005)[69]'s effective field theory to study kerogen effect on the shale anisotropy. Mavko and Saxena (2016) [55] introduced a viscoelastic rock physics model applicable for modeling organic-rich shales. Zhang et al. (2016) [85] compared several rock physics models, and used them in combined for modeling organic rich shales. Bandyopadhyay (2009) [9], Qin et al. (2014) [65], Zhao et al. (2016) [86], and Al Ibrahim and Mukerji (2017) [1] applied the anisotropic DEM algorithm to model elastic property changes of organic-rich shales as they undergo oil and gas windows, and concluded that the mineralogy, TOC, and distribution of kerogen bodies are crucial in determining the elastic properties of the source rock.

1.4 Dissertation organization

The remaining dissertation is organized as follows. In Chapter 2, I will introduce an improved 3D model that estimates the amount of overpressure associated with hydrocarbon generation during the source rock thermal maturation. The 3D model essentially describes a single kerogen lens embedded in an inorganic source rock matrix. As the thermal maturation takes place, the kerogen converts into hydrocarbons, causing an overpressure in the source rock system that can eventually lead into the initiation and propagation of a single microcrack. I will quantify the microcrack initiation and growth, where I use different constitutive equations to describe the physical behaviors of hydrocarbons under laboratory and geological conditions, respectively. This piece of work has been published as Yang and Mavko, 2018 [82] in *AAPG Bulletin*. In Chapter 3, I will introduce a workflow that incorporates geochemical data, especially the data collected from the hydrous pyrolysis experiments to better constrain the rock physics model for estimating elastic properties of the source rock system. By incorporating data acquired from hydrous pyrolysis, elastic property changes of source rocks due to hydrocarbon generation can be better quantified throughout the thermal maturation process. This piece of work is an improvement based on the modeling work published as Yang and Mavko, 2018 [81] in *SEG Technical Program Expanded Abstracts 2018*. Chapter 4 will be focusing on a different topic, where I will introduce a new deep learning based method to classify seismic facies from 3D seismic data. In particular, I will introduce an improved 3D convolutional neural network architecture that leads to more efficient training procedure. This approach proves to be very promising in making geologically reasonable and consistent predictions of seismic facies. Finally, I will summarize what we learned in Chapter 5, and provide directions for future work.

Chapter 2

Microcrack growth in source rocks

2.1 Introduction

In this chapter, we introduce an improved 3D model that estimates the amount of overpressure associated with hydrocarbon generation during kerogen thermal maturation, and predict the behavior of microcrack initiation and growth caused by this overpressure. We differentiate the physical behavior of hydrocarbons under laboratory and geological conditions: hydrocarbons exhibit a pure vapor phase in the laboratory and a pure liquid phase under geological conditions. Under natural geological conditions, the end products of kerogen thermal maturation are more complex: they can be a mixture of oil and gas depending on kerogen types, maturities, and in-situ conditions; we used a simplified one-phase hydrocarbon product assumption to represent the major component resulting from most primary cracking processes. The mechanical properties of each component also vary between laboratory and geological conditions; at elevated temperatures as in the laboratory settings, the modulus of each component is expected to be reduced [27]. The overpressure and microcrack growth are predicted using a combination of geological parameters, hydrocarbon-generation kinetics, elasticity, and principles of linear elastic fracture mechanics (LEFM). The model is used to simulate

(1) laboratory conditions (which refer to the experimental settings described by [42]) and (2) geological conditions where kerogen thermal maturation takes place over geologic time as the sediments are deposited at a constant sedimentation rate.

2.2 Models and problem formulation

In our model shown in Figure 2.1, the organic shale system is treated as a kerogen-filled spherical "pore" of radius R, embedded in a shale matrix. Note that in this chapter, we define the "pore space" as the volume occupied by the organic part, which can be filled by both the solid kerogen and liquid hydrocarbons. Initially, the pore space contains only kerogen and water, with volumetric fractions $(1 - S_w)$ and S_w, respectively, where S_w is the water saturation. The system is subjected to a far-field confining stress σ_0 acting along the vertical direction as one of the principal directions, and is calculated as the lithostatic stress accumulated from zero at $t = 0$, normal to the bedding planes. We adopt the sign convention that a positive value represents compression; this means that $\sigma_0 > 0$. In most SEM images of organic pores [46, 52], horizontal microcracks are dominant in the system despite the fact that vertical confining stress is usually thought to be the greatest. We interpret these images as indicators of the fact that the fracture toughness of the shale matrix is anisotropic, which is supported experimentally by [17]. It is possible to imagine a case where such anisotropies promote the propagation of the cracks along the bedding planes (because the fracture toughness is lowest perpendicular to those planes). The stiffness tensor of the shale background, for simplicity, is regarded as homogeneous and isotropic. Under sufficient overpressure, cracks are created and form an axi-symmetric fracture plane with an axis of symmetry normal to the bedding planes.

The water in the pore has a pressure of p_H, which is assumed to be hydrostatic in the reference state before kerogen maturation takes place. As the kerogen matures, part

of the pore space is taken up by hydrocarbons. Because the generated hydrocarbon has a lower density than kerogen, overpressure $\Delta P = p_p - p_H$ is generated, where p_p is the pore pressure; this tends to expand the pore space and lead to the propagation of cracks. In our model, we assume pre-existing defects of length L_0 around the pore, which is approximately of the same order of magnitude as the surrounding grain size. These defects initially have zero aperture, but under excessive overpressure they can grow into microcracks and create additional pore space. With more pore space to accommodate the hydrocarbons, overpressure drops and crack propagation eventually terminates.

The shale matrix is characterized by its density $\rho_{sh,i}$, drained Young's modulus E_{sh}, Poisson's ratio ν_{sh}, and Mode I fracture toughness K_{Ic} across the bedding planes. The rock mineral is characterized by its bulk modulus K_s. The kerogen and water in the pore space have bulk moduli of K_k and K_w, respectively. The bulk modulus of the hydrocarbon varies between the laboratory and the geologic settings. In the laboratory, because of the elevated temperature and lack of confining stresses, generated hydrocarbons resulting in the overpressure are in the vapor phase and approximately follow the ideal gas law, meaning that the bulk modulus of the hydrocarbon, K_{HC}, is equal to the pore pressure p_p [54]. The total number of moles of hydrocarbons that can be generated per unit volume of kerogen, $n/V_{k,i}$, is specified by the chemical reaction of kerogen maturation. This parameter is also termed the volume expansion parameter under laboratory conditions. Under geologic settings, we consider the hydrocarbons to be in the liquid phase with a constant K_{HC}. Before the development of overpressure, in-situ kerogen and hydrocarbons have densities of $\rho_{k,i}$ and $\rho_{HC,i}$, respectively, under the same ambient pressure. The ratio, $D = \rho_{k,i}/\rho_{HC,i}$, is the volume expansion parameter for geological conditions associated with hydrocarbon generation. The subscript i denotes the reference state where the system is subjected to confining stresses σ_0 from outside and a pore pressure p_H from inside. Finally, the

shale matrix is assumed to be impermeable.

Under laboratory conditions, we have confining stress (pressure) of 1 atm and temperature T increasing linearly from 60 °C to 400 °C at a rate of 1 °C/min. Those laboratory conditions are identical to [42]. Because free water has evaporated at such a temperature, the original volume of water in the pore space is taken up by void space. The K_w is thus irrelevant and $p_H = 1$ atm. Under geological conditions, σ_0, p_H, and T increase linearly over geologic time because of assumed constant burial rate S (m/m.y.), heating rate H (°C/m.y.) associated with burial, and overburden density ρ_{ob}.

2.2.1 Determination of overpressure

Increased overpressure is the primary driver of microcrack development and propagation in our model. Overpressure is calculated differently in the laboratory than in geological settings. Because we assume that hydrocarbons are governed by the ideal gas law in the laboratory, but instead assume linear elasticity in geological settings, we present two different formulations, one for each case. Note that the following overpressure calculations apply to time steps before crack opening and propagation; they are modified when the cracks open and provide additional pore space.

Geologic setting

The determination of overpressure in the geological setting essentially s modified after [11, 15]. At any point in time during the kerogen-to-hydrocarbon transformation, a certain fraction s of the original kerogen has been converted to hydrocarbons. Generally speaking, s is a linear function of the kerogen transformation ratio, which is determined from the hydrocarbon-generation kinetics. Maximum transformation ratio is determined by the kerogen type. Under conservation of mass in the reference

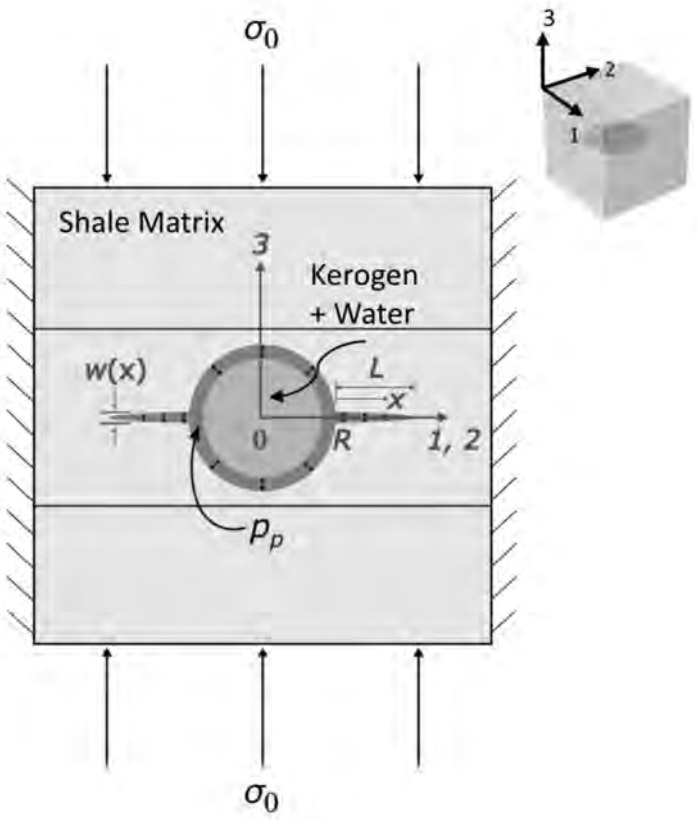

Figure 2.1: Side-view of the 3D source rock system at transformation ratio TR greater than zero, and a 3D schematic on the upper right. At zero TR, the crack aperture is zero; the kerogen and water fill the pore space. At the end of thermal maturation, 30% of the kerogen and residual solid remain in the system. At some TR greater than zero, the microcrack reaches a final length of L_f, with a crack aperture profile $w(x)$. The associated overpressure ΔP is given by $p_f - p_H$, which is the difference between the pore pressure p_p and the reference hydrostatic pressure. σ_0 = confining stress, which is the lithostatic stress accumulated from zero at $t = 0$; L = length; R = radius.

state, we have

$$s\rho_{k,i}V_{k,i} = \rho_{HC,i}V_{HC,i}, \tag{2.1}$$

where $V_{k,i}$ and $V_{HC,i}$ are in-situ volumes of kerogen and hydrocarbon in the reference state. Invoking the definition of volume expansion parameter, D, Eqn.(2.1) becomes

$$\frac{V_{HC,i}}{V_{p,i}} = sD(1 - S_w) \tag{2.2}$$

where $V_{p,i}$ is the initial volume of the pore space given by $V_{p,i} = 4\pi R^3/3 = V_{k,i}/(1-S_w)$.

Because of volume expansion of hydrocarbons and associated loss of kerogen, the net change of the pore space is calculated as

$$\Delta V_p = \Delta V_w + (1 - s)\Delta V_k + \Delta V_{HC} + V_{HC,i} - sV_{k,i}. \tag{2.3}$$

The first three terms in the right side of Eqn.(2.3) are elastic deformations (ΔV) of the water, remaining kerogen volume, and hydrocarbon volume in the pore space, respectively, which are caused by overpressure; the last two terms denote intrinsic volume change associated with kerogen- to-hydrocarbon conversion independent of the overpressure. Dividing Eqn.(2.3) by $V_{p,i}$, and invoking the definition of bulk modulus for linear elastic materials and ignoring the thermal expansion, the bulk moduli of the pore space, water, hydrocarbon, and kerogen, in sequence, are given by $K_p = V_{p,i}\Delta P/\Delta V_p$; $K_w = -V_{w,i}\Delta P/\Delta V_w$; $K_{HC} = -V_{HC,i}\Delta P/\Delta V_{HC}$; and $K_k = -V_{k,i}\Delta P/\Delta V_k$. Substituting the above constitutive relations into Eqn.(2.3), we obtain an expression for ΔP

$$\Delta P = \frac{s(1 - S_w)(D - 1)}{1/K_p + 1/K_{sm}} \tag{2.4}$$

where K_{sm} is the effective bulk modulus of the "soft material" in the pore space

consisting of water, kerogen and hydrocarbons, and is given by

$$\frac{1}{K_{sm}} = \frac{S_w}{K_w} + \frac{(1-s)(1-S_w)}{K_k} + \frac{sD(1-S_w)}{K_{HC}}, \tag{2.5}$$

and K_p is the pore stiffness which can be derived from the porosity, bulk modulus, and grain modulus if we assume that the rock matrix is effectively homogeneous, isotropic, and linear elastic [35]:

$$K_p = \frac{\phi_0}{1/K_{sh} - (1+\phi_0)/K_s} \tag{2.6}$$

where ϕ_0 is the porosity of the shale matrix in the reference state, K_{sh} is the drained bulk modulus of the shale matrix and is given by $K_{sh} = E_{sh}/3(1-2\nu_{sh})$. In the case where S_w and TOC (wt.%) are given, porosity can be calculated as

$$\phi_0 = \frac{\text{TOC}}{0.83 \times 100(1-S_w)} \frac{\rho_{sh,i}}{\rho_{k,i}}, \tag{2.7}$$

where the coefficient 0.83 converts the TOC into total organic matter by wt.% [30].

Laboratory setting

In the laboratory setting, transient hydrocarbon pressure P_0 is determined for the time at which hydrocarbon is first generated from a volume $sV_{k,i}$ of kerogen. The generated hydrocarbon is confined within the volume $sV_{k,i}$ and no elastic deformation is allowed at this this transient time. The transient hydrocarbon pressure is calculated as

$$P_0 = \frac{sn}{sV_{k,i}} RT, \tag{2.8}$$

where n is the total number of moles of hydrocarbons that can be generated from the kerogen of volume $V_{k,i}$. The ratio $n/V_{k,i}$ can be determined from the kerogen-to-hydrocarbon reaction, which is assumed to be unchanged throughout kerogen-to-hydrocarbon reaction. Note that P_0 is associated with the transient hydrocarbon

volume $V_0 = sV_{k,i}$. Because laboratory pyrolysis experiments are performed at temperatures near 400 °C at which the water has evaporated, we make the assumption that $p_H = \sigma_0 = 1$ atm. Because the water has evaporated, the volume $S_w V_{p,i}$, which used to be filled by water, is now void and can be filled by hydrocarbons. After elastic deformation, the final volume of hydrocarbons is given by

$$V_1 = V_{p,i}\left[s(1-S_w) + S_w + \Delta P\left(\frac{(1-s)(1-S_w)}{K_k} + \frac{1}{K_p}\right)\right] \tag{2.9}$$

where ΔP is the "effective pressure", given by the difference between the final pore pressure P_1 and the hydrostatic pore pressure p_H: $\Delta P = P_1 - p_H = P_1 - \sigma_0$. Following the ideal gas law, we obtain an expression with one unknown P_1, which can be solved using the quadratic formula

$$P_1 = P_0 s(1-S_w)\left[s(1-S_w) + S_w + (P_1 - \sigma_0)\left(\frac{(1-s)(1-S_w)}{K_k} + \frac{1}{K_p}\right)\right]^{-1}. \tag{2.10}$$

2.2.2 Framework of fracture mechanics

The initiation and propagation of microcracks are controlled by the Stress Intensity Factor (SIF) at the tip of pre-existing defects. If the net tensile stress is high enough to cause the SIF to exceed the fracture toughness of the shale, K_{Ic}, cracks will open and grow. If we assume that no shear exists, a Mode I (tensile) fracture is initiated if the pore pressure is sufficiently high. The cracks reach equilibrium and stop growing when SIF= K_{Ic}. For the 3D geometry assumed by our model, the general form of the Mode I SIF is given by [58] as

$$K_I = \frac{2}{\sqrt{\pi}}\sigma\sqrt{L}\int_0^L f\left(\frac{x}{L}, \frac{L}{R}\right)\frac{dx}{\sqrt{L^2 - x^2}}, \tag{2.11}$$

where σ is the net tensile stress given by $\sigma = p_p - \sigma_0$, L is the length of the crack starting from the rim of the spherical pore, and x is the position along the crack over length L as shown in Figure 2.1. The function $f\left(\frac{x}{L}, \frac{L}{R}\right)$ adjusts the coefficient for cracks with different lengths, and is given by

$$f\left(\frac{x}{L}, \frac{L}{R}\right) = \frac{x/L + R/L}{1 + R/L}\left(1 + 0.3\left(1 - \frac{x}{L}\right)\left(\frac{1}{1 + L/R}\right)^6\right). \tag{2.12}$$

In the limiting cases for short and long cracks, Eqn.(2.11) gives SIFs for notch- and penny-shaped cracks, respectively.

A common criterion for quasistatic fracture propagation in the framework of LEFM is given by

$$SIF \geq K_{Ic}. \tag{2.13}$$

At the moment when defects start to grow into cracks, the following relationship holds

$$K_{Ic} = \frac{2}{\sqrt{\pi}}(p_p - \sigma_0)\sqrt{L_0}\int_0^{L_0} f\left(\frac{x}{L_0}, \frac{L_0}{R}\right)\frac{dx}{\sqrt{L_0^2 - x^2}} \tag{2.14}$$

where $p_p = \Delta P + p_H$, and can be determined from Eqns.(2.4) and (2.10). At the end of the crack propagation process, the SIF at the crack tip once again equals fracture toughness of the shale matrix, where final pore pressure p_f and crack length L_f are found. We can show that the crack propagation can eventually terminate, because the pore pressure reduction rate, $\partial p_p/\partial L$, is larger than $\partial L^{1/2}/\partial L$ in the long crack limit, ensuring that SIF decreases as the crack length L grows in the limiting case; a sketch of proof is given in the Appendix.

To solve for the final pore pressure p_f and crack length L_f at equilibrium, we must evaluate the extra pore space V_{cr} created by crack opening. Because of the axi-symmetric nature the source rock system, we can calculate V_{cr} by integrating the crack aperture profile around the axis of symmetry. The aperture of the crack (twice

the displacement of a single surface on the crack) is given by

$$w(x) = \frac{4}{\pi}\frac{(1-\nu_{sh})(p_p-\sigma_0)}{G_{sh}}\int_x^L \left[\int_0^a f\left(\frac{\xi}{a},\frac{a}{R}\right)\frac{d\xi}{\sqrt{a^2-\xi^2}}\right] f\left(\frac{x}{a},\frac{a}{R}\right)\frac{a+R}{x+R}\frac{ada}{\sqrt{a^2-x^2}}. \tag{2.15}$$

where G_{sh} is the shear modulus of the shale matrix given by $E_{sh}/2(1+\nu_{sh})$. It follows that V_{cr} is calculated as

$$V_{cr} = \int_0^L 2\pi(R+x)w(x)dx. \tag{2.16}$$

Note that V_{cr} is a function of p_p and L. When the cracks stop propagating, $V_{cr} = V_{cr}(p_f, L_f)$.

Determination of final pore pressure and crack length

In the geological settings, after the formation of fracture plane, Eqn.(2.3) becomes

$$\Delta V_p + V_{cr} = \Delta V_w + (1-s)\Delta V_k + \Delta V_{HC} + V_{HC,i} - sV_{k,i}. \tag{2.17}$$

Substituting the constitutive relations, the expression for final pore pressure p_f considering crack volume becomes

$$p_f = \frac{s(1-S_w)(D-1) + V_r(p_f,L_f)\sigma_0 + (1/K_p + 1/K_{sm})p_H}{V_r(p_f,L_f) + 1/K_p + 1/K_{sm}} \tag{2.18}$$

where $V_r(p_f, L_f)$ is the normalized crack volume divided by the effective tensile stress, namely $V_r(p_f,L_f) = V_{cr}(p_f,L_f)/(p_f-\sigma_0)V_{p,i}$. Meanwhile, the crack opens and propagates critically when the SIF reaches fracture toughness. The fracture criterion is met when the crack stops propagating, where the pore pressure and crack length

reach p_f and L_f, respectively,

$$K_{Ic} = \frac{2}{\sqrt{\pi}}(p_f - \sigma_0)\sqrt{L_f}\int_0^{L_f} f\left(\frac{x}{L_f}, \frac{L_f}{R}\right)\frac{1}{\sqrt{L_f^2 - x^2}}dx. \tag{2.19}$$

We can solve for p_f and L_f using Eqns.(2.18) and (2.19) for the geological setting.

In the laboratory setting, with the additional pore volume contributed from the microcrack volume, the final hydrocarbon volume becomes

$$V_f = V_{p,i}\left[s(1 - S_w) + S_w + (p_f - \sigma_0)\left(V_r(p_f, L_f) + \frac{(1-s)(1-S_w)}{K_k} + \frac{1}{K_p}\right)\right] \tag{2.20}$$

and Eqn.(2.10) becomes

$$p_f = \left[s(1 - S_w) + S_w + (p_f - \sigma_0)\left(V_r(p_f, L_f) + \frac{(1-s)(1-S_w)}{K_k} + \frac{1}{K_p}\right)\right]^{-1} s(1 - S_w)P_0. \tag{2.21}$$

We can solve for p_f and L_f using Eqns.(2.21) and (2.19) for the laboratory setting.

2.3 Numerical results

We created a Matlab simulator implementing Eqns.(2.1)-(2.21), and ran the simulation in both laboratory and geological settings. A comparison between the simulation and the experimental results by [42] were made, followed by a series of parametric studies. The shale properties were based on the Eocene Green River shale sample from Piceance Basin in Colorado, which was used by [42]. Burnham and Braun (1990) [13] and Peters et al. (2016) [62] compiled extensive kinetics parameters for the Green River shale so we made our selection based on those references with calibration to the experiment

by [42]. Mechanical properties of the shale were estimated and adjusted according to [20] and [27]. For the geological setting, we selected typical sedimentation rate, heating rate, and average overburden density to simulate natural microcrack growth over geologic time. Input parameters are given in Table 2.1. The main differences between the two settings, apart from differences in mechanical properties because of temperature effects, lie in the confining stress and ambient temperature.

2.3.1 Parameters for hydrocarbon-generation kinetics

The hydrocarbon-generation kinetics follow the typical type I kinetics, which is applicable to Eocene Green River shale in the Piceance Basin. The transformation ratio, TR, of kerogen maturation is described by a first-order ordinary differential equation and the reaction rate k is approximated by the Arrhenius equation

$$\frac{d\mathrm{TR}}{dt} = k(1 - \mathrm{TR}), \tag{2.22}$$

$$k = A \exp(-E_a/RT), \tag{2.23}$$

where A is the preexponential factor and E_a is the activation energy. We used $A = 5 \times 10^{13}\,\mathrm{s}^{-1}$ and $E_a = 49$ kcal/mol after [13] and [62]. At the end of the kerogen transformation, 30% of the original mass typically remains so that $s = 0.70\mathrm{TR}$ for the volume fraction of decomposed kerogen at any time t where TR ranges from 0 to 1.

2.3.2 Parameters for the geologic setting

The parameters for geological settings are primarily based on normally compacted sedimentary rock formations. In the reference state, pore pressure is assumed to be hydrostatic

$$p_H(t) = \rho_H g S t \tag{2.24}$$

where ρ_H is the water density, S is the constant sedimentation rate, g is the acceleration of gravity, and t is the geologic time. For the case study, $\rho_H = 1000$ kg/m^3, $S = 100$ m/m.y., and $g = 9.81$ m/s^2.

The temperature profile is given by

$$T(t) = T_0 + Ht, \tag{2.25}$$

where T_0 is the surface temperature (25 °C), and H is the constant heating rate (2.5 °C/m.y.). The confining stress, σ_0, which is the lithostatic stress accumulated from zero at $t = 0$, is given by

$$\sigma_0(t) = \rho_{ob} g S t, \tag{2.26}$$

where ρ_{ob} is the average density of the overburden taken as 2200 kg/m^3. Note that in all examples, the temperature, confining stress, and reference pore pressure all increase linearly with geologic time.

Typically, parameters such as the Young's modulus, Poisson's ratio, and fracture toughness are measured at room temperature. In reality, mechanical properties of each component change as a function of temperature. For example, Closmann and Bradley (1979) [20] report that Young's modulus of an oil shale decreases as the temperature increases. At approximately 100 °C, where kerogen maturation is active, Young's modulus of an oil shale is expected to be approximately 40% of the modulus measured at ambient conditions. As a result, we scaled the Young's modulus reported by [18], as well as bulk moduli for the other constituents, by 40% to represent conditions in the oil window. Poisson's ratio remains 0.3 for the shale matrix. The actual values used are shown in Table 2.1.

2.3.3 Parameters for laboratory setting

The laboratory conditions were set based on the experimental setup of [42]. The ambient temperature linearly increased at a rate of 1 °C/min from 60 °C to 400 °C. No external confining pressure was applied to the shale sample; it was set to be 1 atm to be consistent with the reference pressure in the pore space. Because the products from kerogen thermal maturation approximately follow the ideal gas law, we use the number of moles of gas generated per unit volume of original kerogen, $n/V_{k,i}$, to evaluate the instantaneous overpressure caused by the tendency of volume expansion. Note that products generated by kerogen maturation contain non-hydrocarbon substances; we took this into consideration in the calculation of $n/V_{k,i}$. In the experiments conducted by [42], the sample forms horizontal microcracks with aperture sizes between 5 and 25 µm upon heating to 350 °C. Based on the heating procedure used in that study, we can estimate the composition of the end product, which consists of a mixture of oil and gas. The densities of the oil and kerogen, for the first-order approximation, can be treated as roughly equal, so that the generated oil does not contribute the overpressure. The gas mixture, however, approximately follows the ideal gas law, and has a much larger density difference from the kerogen and oil. From [71] and [12], the gas composition corresponding to the oil yield of the current experiment is approximately 20.0 mol% CH_4, 21.0 mol% CO_2, and 34.0 mol% H_2. Additionally, we added 5.0 mol% CO as one of the non-hydrocarbon products. To determine the average composition of the remaining 20.0 mol% hydrocarbon gas, we assumed an approximately 1:1 weight ratio between the hydrocarbon and non-hydrocarbon gases, and obtained an average composition of $C_{2.5}H_{10}$. The complete gas mixture composition is given in Table 2.2, which has an average molecular weight of 22.5 amu. For an average kerogen density of 1100 kg/m^3, $n/V_{k,i}$ is approximately 0.05 mol/cm^3 for this given gas mixture. For the parametric study, we use three sets of $n/V_{k,i}$ values, ranging from 0.02 mol/cm^3 to 0.06 mol/cm^3, to calculate the final overpressure and

crack lengths.

For a temperature range of 300 °C to 400 °C, where microcracks open and propagate, the moduli of each constituent are reduced to 10% of the moduli measured at room temperature, as suggested by [20]; the values are tabulated in Table 2.1.

2.4 Discussion

2.4.1 Comparison with laboratory results

Figure 2.2 shows a comparison between our simulation results and the experimental data of [42]. The top panel shows the fracture surface area as a function of the heating temperature. The circles were extracted from the experimental data of [42], where they measured the largest fracture surface area in the sample. In our simulation, we used a fracture toughness of the shale matrix of 0.05 MPa-m$^{1/2}$, an initial pore radius of 38 mm, and a volume expansion parameter, $n/V_{k,i}$, of 0.04 mol/cm^3. Our simulation results were able to match the experimental data reasonably well. The middle and bottom rows show additional simulation results of the overpressure and crack sizes as functions of the transformation ratio. We observed a few megapascals residual overpressure at the end of maturation because the system is assumed to be impermeable. The crack reached a length of 2 mm, a median crack aperture of 3.6 µm, and a crack volume approximately 180 times the original pore volume at a final temperature of 400 °C. Note that our crack aperture estimate is smaller than the observations made by [42], where the crack apertures ranged between 5 and 25 µm. Possible explanations include (1) difference in the average kerogen particle size, (2) fracture enhancement because of interactions among multiple kerogen bodies and microcracks, and (3) different mechanical properties for shale matrix and the kerogen. Finally, we note that the $n/V_{k,i}$ value of 0.04 mol/cm^3 is reasonable if the products

generated from the kerogen maturation are primarily gases.

We performed parametric studies in both laboratory and geological settings. The parameters of interest include the volume expansion parameter, which is $n/V_{k,i}$ in the laboratory setting and D in the geological setting, the radius of the initial pore space, R, the fracture toughness of the shale matrix, K_{Ic}. For each parametric study, we calculated the fracture surface area, A; the overpressure, ΔP; final crack length, L_f; the median of crack apertures, w_{med}; and the secondary porosity contributed through the crack opening normalized by initial pore volume, $V_{cr}/V_{p,i}$.

2.4.2 Parametric studies in laboratory settings

Figure 2.3 shows the results of our parametric study for the $n/V_{k,i}$ ratio under laboratory settings. We fixed the fracture toughness at 0.05 MPa-m$^{1/2}$, and the initial pore radius at 40 mm. In cases where $n/V_{k,i}$ is 0.04 mol/cm^3 and 0.06 mol/cm^3, crack propagation has already taken place at 300 °C. For a smaller $n/V_{k,i}$ ratio of 0.02 mol/cm^3, overpressure accumulation is slower so that crack propagation is delayed, which takes place at an approximate temperature of 305 °C represented by the jump in the median of crack aperture in Figure 2.3 (D). Once cracks are formed, the final overpressures are approximately the same in all of the cases, approximately 12 MPa above the ambient pressure, because the vapor products are not allowed to escape from the system. The $n/V_{k,i}$ has a large effect in determining the final crack sizes. For an $n/V_{k,i}$ of 0.02 mol/cm^3, the crack reaches a final length of 1.5 mm, a median of crack apertures of 3 µm, and a fracture surface area of 7.5 mm^2, resulting in a crack volume approximately 50 times larger than the original pore volume. For larger $n/V_{k,i}$ values, the crack sizes grow, with an $n/V_{k,i}$ of 0.06 mol/cm^3, the fracture surface area is approximately 23 mm^2 with a crack volume more than 200 times larger than the original pore volume, resulting in a large amount of secondary porosity.

Figure 2.4 shows the sensitivity of results to the initial pore size. Because of

the dimensional dependence of the SIF on the crack length, smaller pores generate much smaller cracks. For instance, comparing $R = 20$ mm and $R = 60$ mm, the final fracture surface areas are 2.0 mm^2 and 50 mm^2, respectively, the final crack lengths are 0.80 mm and 4.0 mm, respectively, and the medians of crack apertures are 2 µm and 4.5 µm, respectively. Consequently, secondary porosity (V_{cr}) is correlated with the initial pore size. The overpressure is also related to the initial pore size because it is approximately inversely proportional to the crack length accordingly to the formula of the SIF and fracture propagation criterion. Smaller pores result in shorter cracks and thus larger overpressures.

Figure 2.5 shows the sensitivity to the fracture toughness. We observe that low fracture toughness samples are prone to fracture and grow long cracks and large crack volumes. For instance, for a K_{Ic} of 0.05 MPa-m$^{1/2}$, the final crack length is approximately 2.0 mm with a crack volume almost 150 times larger than the original pore volume. The associated overpressure is small, only approximately 1 MPa, compared to 5 MPa for K_{Ic} of 0.15 MPa-m$^{1/2}$. Because the overpressure is small, the crack aperture is small too (around 3 µm), but this effect is overshadowed by a much longer crack that still gives a larger fracture surface area and crack volume overall. In contrast, for a K_{Ic} of 0.15 MPa-m$^{1/2}$, the associated crack length, fracture surface area, and crack volume are much smaller, whereas the final overpressure is larger. In addition, the fracture toughness also affects the onset of crack propagation. For a value of 0.05 MPa-m$^{1/2}$, crack propagation has already taken place at 300 °C. In contrast, crack propagation does not occur until reaching a temperature of 320 °C for a fracture toughness of 0.15 MPa-m$^{1/2}$. In summary, the overpressure, the onset of crack propagation, and crack sizes are all sensitive to the fracture toughness.

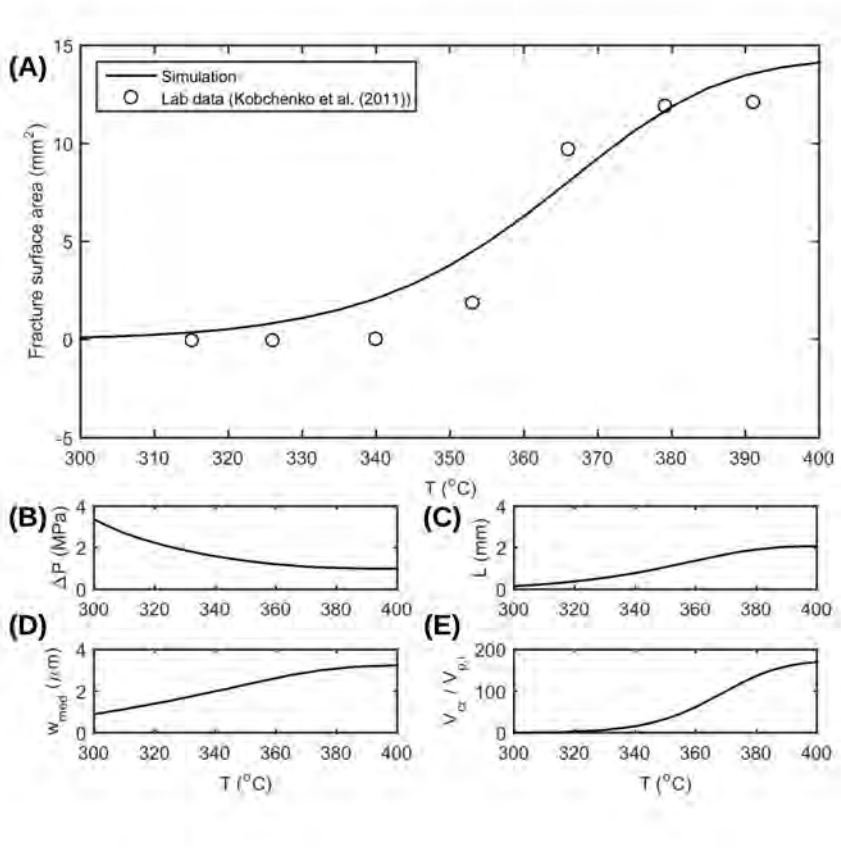

Figure 2.2: Comparison with the experimental data of [42]. (A) The fracture surface area as a function of the heating temperature. Data points were extracted from [42]; black curves were obtained from our simulation results. Underneath the fracture surface area, overpressure (ΔP; B), crack length (L; C), median of crack apertures (w_{med}; D), and crack volume normalized by initial pore volume($V_{cr}/V_{p,i}$; E) were plotted against the heating temperature T.

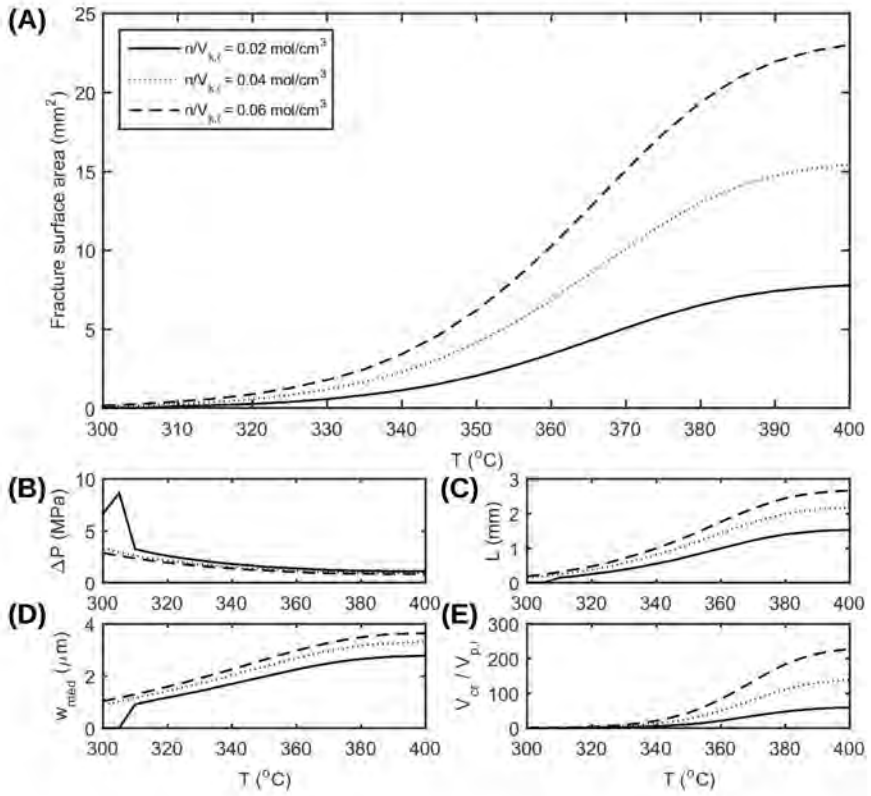

Figure 2.3: Parametric study of the volume expansion parameter, $n/V_{k,i}$, in laboratory conditions. (A) The fracture surface area as a function of the heating temperature T. Overpressure (ΔP; B), crack length (L; C), median of crack apertures (w_{med}; D), and crack volume normalized by initial pore volume ($V_{cr}/V_{p,i}$; E) were plotted against the heating temperature T. Three curves with various $n/V_{k,i}$ ratios were plotted. The pore radius R is 40 mm, and the fracture toughness K_{Ic} is 0.05 MPa-m$^{1/2}$.

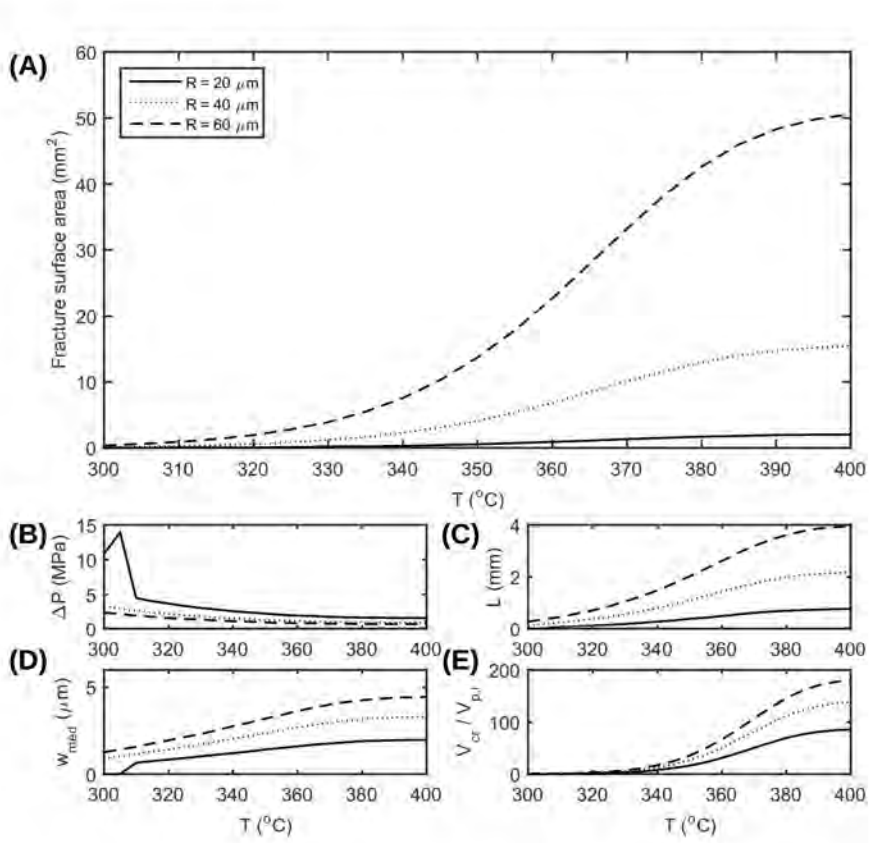

Figure 2.4: Parametric study of the initial pore radius, R, in laboratory conditions. (A) The fracture surface area as a function of the heating temperature T. Overpressure (ΔP; B), crack length (L; C), median of crack apertures (w_{med}; D), and crack volume normalized by initial pore volume ($V_{cr}/V_{p,i}$; E) were plotted against the heating temperature T. Three curves with various R values were plotted. The volume expansion parameter $n/V_{k,i}$ is 0.04 mol/cm^3, and the fracture toughness K_{Ic} is 0.05 MPa-m$^{1/2}$.

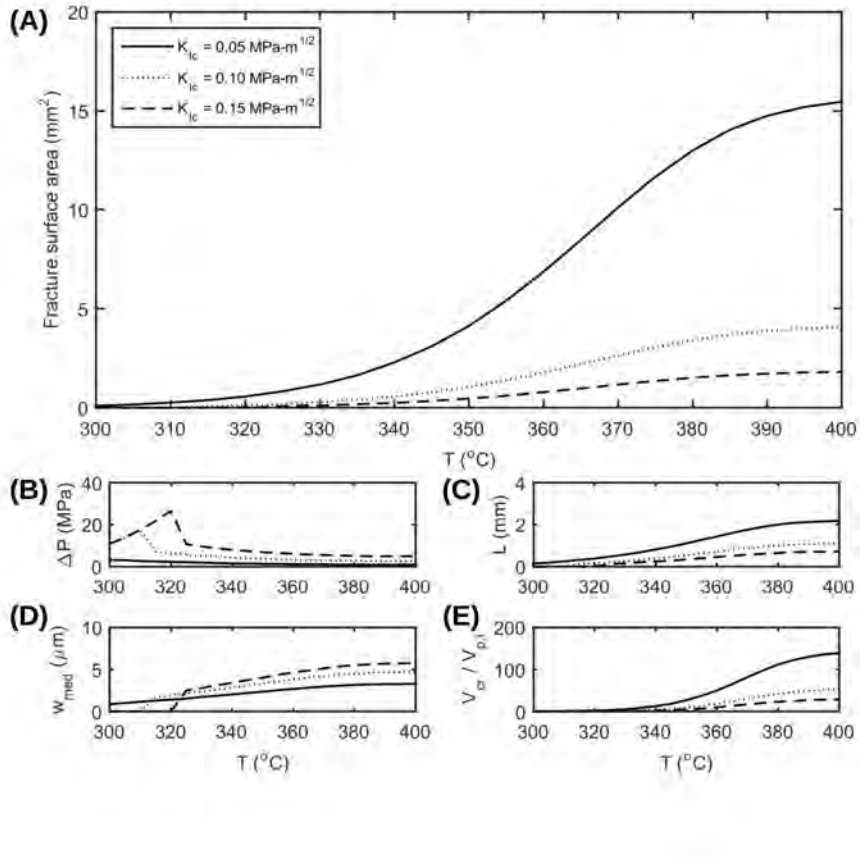

Figure 2.5: Parametric study of the fracture toughness, K_{Ic}, in laboratory conditions. (A) The fracture surface area as a function of the heating temperature T. Overpressure (ΔP; B), crack length (L; C), median of crack apertures (w_{med}; D), and crack volume normalized by initial pore volume ($V_{cr}/V_{p,i}$; E) were plotted against the heating temperature T. Three curves with various K_{Ic} values were plotted. The pore radius R is 40 mm, and the volume expansion parameter $n/V_{k,i}$ is 0.04 mol/cm^3.

2.4.3 Parametric studies in geological settings

Figures 2.6 - 2.8 show the stress histories and crack growth over geologic time. We primarily focus on the time interval 15 m.y. to 40 m.y., during which the kerogen of specified hydrocarbon-generation kinetics matures. Parametric studies on the volume expansion parameter, D, the initial pore radius, R, and the fracture toughness, K_{Ic}, were performed in the geological settings. In the upper panels of Figures 2.6 - 2.8 where the stress histories are shown, the overburden, σ_0, and the reference pore pressure, p_H, both increase linearly over time. This is because of the constant sedimentation rate, overburden density, and the assumption of hydrostatic pore pressure in the reference state. As the conversion of kerogen to hydrocarbons takes place, the pore pressure, p_f, gradually builds up. It starts from the hydrostatic pore pressure and eventually exceeds the overburden. Because the net tensile stress is calculated as the difference between the pore pressure and the overburden, the pore pressure must exceed the overburden to initiate crack propagation. The amount of net tensile stress needed for crack propagation is determined by the fracture toughness: the lower the K_{Ic}, the lower the net tensile stress needed. At equilibrium when the crack propagation terminates, the SIF is maintained at the level of K_{Ic}, and hence a nearly constant offset between the pore pressure and the overburden is seen in all cases at later maturation stages. In the upper panel of Figure 2.8, we observe larger variation in the amount of offset for different fracture toughness values after crack propagation has taken place. This is because the SIF is proportional to the net tensile stress so that the overpressure is most sensitive to the fracture toughness and relatively less sensitive to the volume expansion parameter and the pore size. Additionally, from the upper panel of Figure 2.6 we also observe that the volume expansion parameter has a large control on the overpressure build-up rate and the onset of crack propagation where the kink in the pore pressure drop is located. For a D of 1.2, crack propagation does not occur until 37 m.y., whereas for a D of 1.6, crack propagation takes place as early as

32 m.y. Results on the effects of volume expansion parameter and fracture toughness are consistent with those produced by [28, 29]; the magnitude of the overpressure is also close.

The four lower panels in Figures 2.6 - 2.8 show the sensitivities of overpressure and microcrack sizes to the volume expansion parameter, the initial pore size, and the fracture toughness as functions of transformation ratio in the geological settings. Because a significant amount of overburden is exerted on these samples, microcrack sizes are much smaller than those in the laboratory settings. This is seen most clearly in the bottom rows of Figures 2.6 - 2.8, where plots of the median of crack apertures and normalized crack volumes are shown. Compared with the apertures of cracks generated under laboratory conditions (on the order of a few microns), apertures of cracks generated under geological conditions are minuscule: below 0.5 µm in all of the cases. As a result, no significant amount of crack volume (secondary porosity) is generated through the formation of the fracture planes. By using larger D values, such as 1.6, we may be able to obtain secondary porosity that is approximately 25% of the original pore volume. Furthermore, we observe that although all the three parameters under study affect the microcrack dimensions, only the volume expansion parameter affects the overpressure build-up rate (Figure 2.6), and that only the fracture toughness considerably affects the final pore pressure (Figure 2.8). In all of the cases, the final crack length lies in the range of hundreds of microns, and the crack aperture lies in the sub-micron range, both of which agree with observations from several SEM images showing in-situ organic-rich shale samples [46, 5].

2.5 Summary

In this chapter, we presented a model that predicts the microcrack growth and pore pressure changes during the process of kerogen thermal maturation in organic-rich

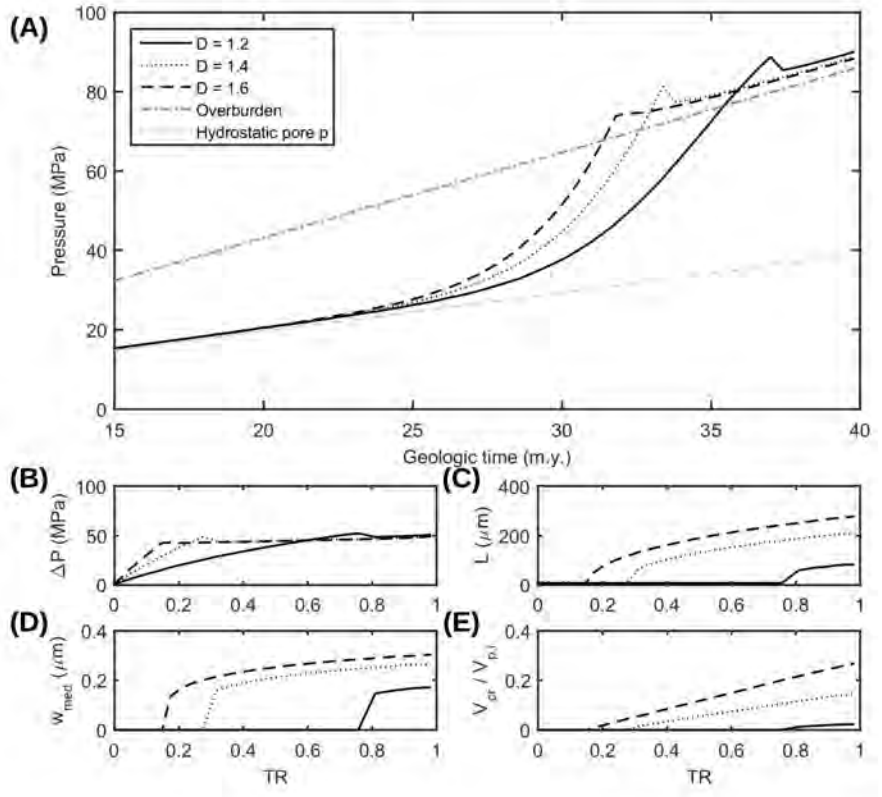

Figure 2.6: Parametric study of the volume expansion parameter D under geological conditions. (A) The stress history plotted against the geologic time. The dark gray broken line denotes the overburden (confining stress, which is the lithostatic stress accumulated from zero at $t = 0$); the light gray broken line denotes the hydrostatic pore pressure p_H in the reference state. Three black curves (solid, dotted, and dashed) with various volume expansion parameters, D, denote the actual pore pressure over time. Underneath the stress history, overpressure (ΔP; B), crack length (L; C), median of crack apertures (w_{med}; D), and crack volume normalized by initial pore volume ($V_{cr}/V_{p,i}$; E) were plotted against the transformation ratio, TR. The pore radius R is 40 mm, and the fracture toughness K_{Ic} is 0.05 MPa-m$^{1/2}$.

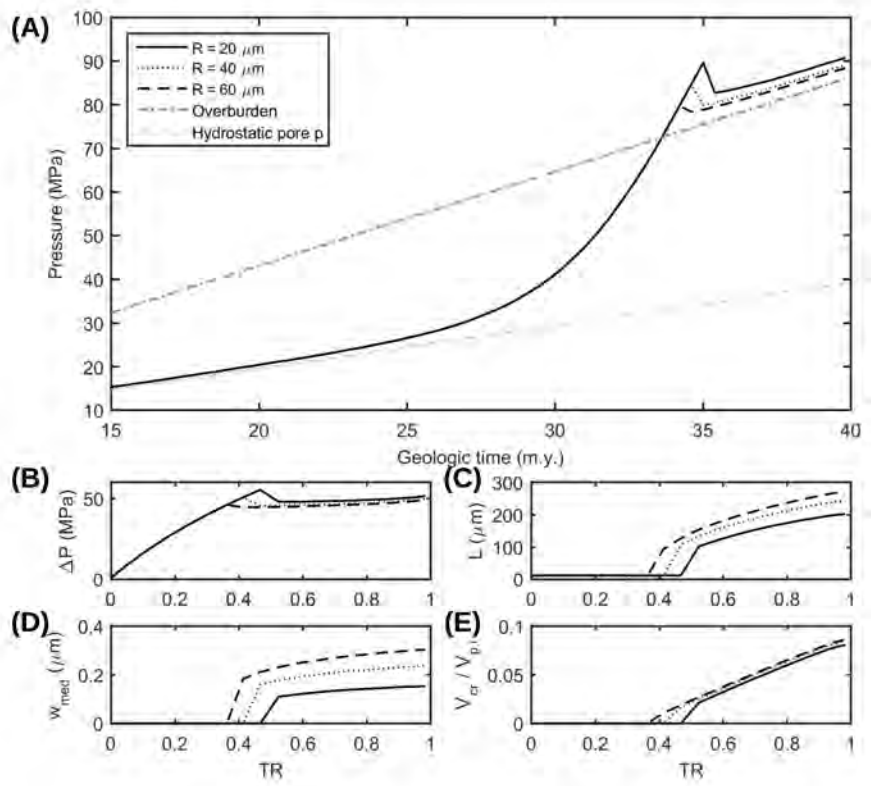

Figure 2.7: Parametric study of the initial pore radius R under geological conditions. (A) The stress history plotted against the geologic time. The dark gray broken line denotes the overburden (confining stress, which is the lithostatic stress accumulated from zero at $t = 0$); the light gray broken line denotes the hydrostatic pore pressure p_H in the reference state. Three black curves (solid, dotted, and dashed) with various initial pore radii, R, denote the actual pore pressure over time. Underneath the stress history, overpressure (ΔP; B), crack length (L; C), median of crack apertures (w_{med}; D), and crack volume normalized by initial pore volume ($V_{cr}/V_{p,i}$; E) were plotted against the transformation ratio, TR. The fracture toughness K_{Ic} is 0.05 MPa-m$^{1/2}$, and and the volume expansion parameter D is 1.3.

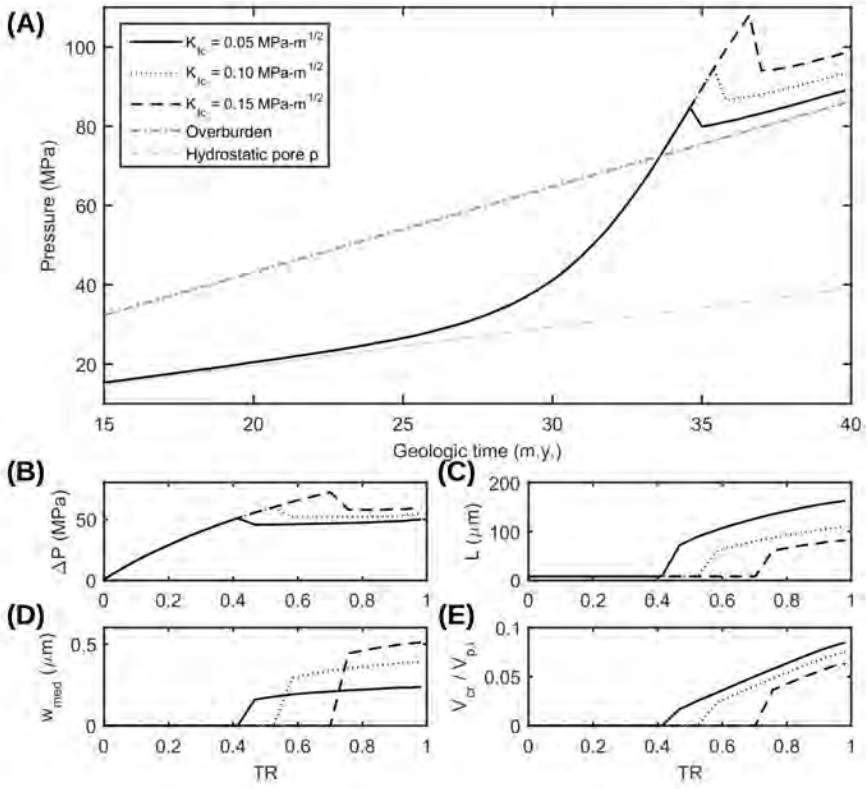

Figure 2.8: Parametric study of the fracture toughness K_{Ic} under geological conditions. (A) The stress history plotted against the geologic time. The dark gray broken line denotes the overburden (confining stress, which is the lithostatic stress accumulated from zero at $t = 0$); the light gray broken line denotes the hydrostatic pore pressure p_H in the reference state. Three black curves (solid, dotted, and dashed) with various fracture toughnesses, K_{Ic}, denote the actual pore pressure over time. Underneath the stress history, overpressure (ΔP; B), crack length (L; C), median of crack apertures (w_{med}; D), and crack volume normalized by initial pore volume ($V_{cr}/V_{p,i}$; E) were plotted against the transformation ratio, TR. The pore radius R is 40 mm, and the volume expansion parameter D is 1.3.

shales. This model is primarily based on elasticity and LEFM. By running the simulation under laboratory conditions, we obtained similar fracture surface areas to those measured by [42]. Secondary porosity generated by crack opening is significant under laboratory conditions: the induced crack volume can accommodate several hundred times the initial pore volume. In contrast, under geological conditions, no significant secondary porosity is generated through crack opening. If the kerogen-to-hydrocarbon density ratio is high enough, overpressure can be built up more quickly, and microcracks can propagate at earlier maturation stages. However, the extent of propagation and resulting apertures are much smaller than those generated under laboratory settings because of the effect of overburden. Parametric studies show that the volume expansion parameter, initial pore size, and fracture toughness of the shale matrix are all major factors in the final microcrack sizes and pore pressures to varying degrees. The comparison between laboratory and geological conditions shows that the source rock system behaves fundamentally differently in those two settings; extrapolation from laboratory to geological settings must be treated with care.

It should be noted that we have assumed that the fracture toughness is anisotropic, and that it attains the lowest value when measured across the bedding planes. The assumptions made crack propagation along the bedding planes favorable. If the mechanical parameters that characterize the shale matrix across the bedding planes vary, we should expect different results for the crack orientation, the microcrack size, and the pore pressure.

The shale matrix is assumed to be impermeable throughout the kerogen thermal maturation. If permeability is present, we would expect the pore pressure to decrease over time and eventually equilibrate with the hydrostatic pore pressure. To maintain the crack opening after the pore pressure drop associated with fluid flow, inelastic deformation in the shale matrix must occur. This would need more comprehensive modeling of the mechanical evolution of host rocks during the kerogen thermal

maturation. The impermeable assumption of our source rock system implies that our model primarily applies to the early hydrocarbon generation and retention stages before any expulsion takes place. The formation of microcracks connects isolated microscale hydrocarbon pockets, providing pathways for the primary migration in later stages.

Additionally, we have used a single pair of activation energy and preexponential factors to characterize the hydrocarbon-generation kinetics. In reality, hydrocarbon-generation kinetics would evolve as the kerogen maturation proceeds, and a more sophisticated model is often used to differentiate the kinetics for primary cracking from the secondary cracking. As a result, the volume expansion parameter, which controls the physical behavior of the generated products, is expected to vary as a function of the transformation ratio. The inclusion of those complexities would be straightforward extensions to the current model.

Last but not the least, we assumed a single kerogen body in the system, which leads to the creation of a single crack plane. If multiple kerogen bodies coexist, they can result in multiple microcracks, which would interact with each other during propagation. In general, the presence of multiple cracks would either enhance or shield the crack propagation depending on the crack position and orientation (Lam and Phua, 1991 [45]). We need to reply on numerical approaches to solve multi-crack problems.

Table 2.1: Parameters for the simulation.

Parameter	**Variable**	**Value**	**Reference**
Common parameters			
Activation energy of kerogen (kcal/mol)	E_a	49	[12]
Preexponential factor (s^{-1})	A	5×10^{13}	[62]
Total organic carbon (TOC) (wt.%)	TOC	9.92	[42]
Ratio of initial defect length to initial pore radius	L_0/R	0.2	
Water (void) saturation	S_w	0.05	
Drained Poisson's ratio of shale	ν_{sh}	0.3	[18]
Density ratio of shale to kerogen	$\rho_{sh,i}/\rho_{k,i}$	2.0	
Parameters for laboratory settings			
Ambient temperature (°C)	T	60-400	[42]
Heating rate (°C/min)	H	1	[42]
Confining stress (MPa)	σ_0	0.1	[42]
Bulk modulus of kerogen (GPa)	K_k	0.83	[84]
Bulk modulus of rock grains (GPa)	K_s	3.90	[54]
Drained Young's modulus of shale (GPa)	E_{sh}	1.00	[20]
Parameters for geological settings			
Surface temperature (°C)	T_0	25	
Sedimentation rate (m/m.y.)	S	100	
Heating rate (°C/m.y.)	H	2.5	
Average overburden density (kg/m^3)	ρ_{ob}	2200	
Water density (kg/m^3)	ρ_w	1000	
Bulk modulus of hydrocarbon (GPa)	K_{HC}	0.68	[54]
Bulk modulus of water (GPa)	K_w	2.73	[54]
Bulk modulus of kerogen (GPa)	K_k	3.32	[84]
Bulk modulus of rock grains (GPa)	K_s	15.6	[54]
Drained Young's modulus of shale (GPa)	E_{sh}	4.00	[20]

Table 2.2: Gas compositions for the laboratory setting.

Gas	mol %	Molar mass (g/mol)
H_2	34.0	2
CO_2	21.0	44
CO	5.0	28
CH_4	20.0	16
$C_{2.5}H_{10}$	20.0	40

Chapter 3

Source rock elastic property estimation

3.1 Introduction

In this chapter, we introduce a workflow that incorporates geochemical data, especially the data from the hydrous pyrolysis to better constrain the rock physics models for estimating elastic properties of the organic-rich source rocks. By incorporating data acquired from hydrous pyrolysis, elastic property changes of source rocks due to hydrocarbon generation can be better quantified throughout the thermal maturation process.

3.2 Methods

3.2.1 Anisotropic DEM algorithm

Organic-rich shale is usually anisotropic due to the fine layered structures exhibited by clay minerals. When modeling the shale, we usually treat the shale as a VTI

structure, where five independent elastic constants completely determine its elastic stiffness tensor. The anisotropic DEM modeling scheme proposed by [59] and [32] provides a tool for estimating the effective elastic stiffness tensor for the mixture where the background matrix is VTI, and the inclusion material is isotropic. The mathematical form of the anisotropic DEM is given by

$$\frac{d\mathbf{C}^{DEM}(v)}{dv} = \frac{\mathbf{C}^{i} - \mathbf{C}^{DEM}(v)}{1-v}\left[\mathbf{I} + \hat{\mathbf{G}}\left(\mathbf{C}^{i} - \mathbf{C}^{DEM}(v)\right)\right]^{-1}, \tag{3.1}$$

where v is the volume fraction of the inclusion at some instance in time, $\mathbf{C}^{DEM}$ is the elastic stiffness tensor of the effective anisotropic medium, $\mathbf{C}^{i}$ is the elastic stiffness tensor of the isotropic inclusions, $\mathbf{I}$ is the fourth-rank identity tensor, and $\hat{\mathbf{G}}$ is a fourth-rank tensor. Jakobsen et al. (2000) [36] expressed $\hat{\mathbf{G}}$ (or $\mathbf{P}$ in their notations) in the form of

$$\hat{G}_{ijkl} = \frac{1}{16\pi}\left(\bar{G}_{ikjl} + \bar{G}_{jkil} + \bar{G}_{iljk} + \bar{G}_{jlik}\right) \tag{3.2}$$

where expressions for $\bar{G}_{ikjl}$ are given explicitly in [9] and [59] for VTI structures.

The anisotropic DEM algorithm starts with an initial condition that $\mathbf{C}^{DEM} = \mathbf{C}_0$, where $\mathbf{C}_0$ is the elastic stiffness tensor of the background matrix defined as the inorganic mineral phases in the shale. The algorithm incrementally adds inclusions into the background matrix, and updates $\mathbf{C}^{DEM}$ according to Eqn.(3.1). The newly added inclusions assume no interactions with previously added inclusions. At the end of the iteration, we obtain the elastic stiffness tensor of the effective medium $\mathbf{C}^{DEM}$ with a total volume fraction ϕ of inclusions.

3.2.2 Batzle-Wang's relation

The Batzle-Wang's relations [10] is a set of empirical equations which are used to estimate density and velocity of hydrocarbon mixtures in the reservoir conditions.

The workflow of estimating elastic properties of hydrocarbons using Batzle-Wang's relation is explained in details in [54]. Here I'm giving an outline of the workflow of applying Baztle-Wang's relation.

First, given the oil density ρ_o in the API unit, we can convert it into g/cm^3 by

$$\rho_o = 141.5/(API + 131.5). \tag{3.3}$$

To add solution gas into the oil, we first estimate the oil formation volume factor B_o (dimensionless)

$$B_o = 0.972 + 3.8 \times 10^{-4}(2.4\sqrt{G/\rho_o} + T + 17.8)^{1.175} \tag{3.4}$$

where G is the gas gravity (dimensionless) of the gas saturated in the oil, and T is the in-situ temperature in °C. The updated density of oil with solution gas, ρ_G (in g/cm^3), is given by

$$\rho_G = (\rho_o + 1.2 \times 10^{-3} G \times GOR)/B_o \tag{3.5}$$

where GOR is the gas-to-oil ratio in m^3/m^3. The final in-situ oil density with solution gas (in g/cm^3) adjusted for pressure and temperature effects is given by

$$\rho = \frac{\rho_P}{0.972 + 3.81 \times 10^{-4}(T + 17.78)^{1.175}} \tag{3.6}$$

where ρ_P is given by

$$\rho_P = \rho_G + (2.77 \times 10^{-3} P - 1.71 \times 10^{-7} P^3)(\rho_G - 1.15)^2 + 3.49 \times 10^{-4} P \tag{3.7}$$

where P is the in-situ pressure in MPa.

To further calculate the P-wave velocity V_p (in m/s) of the fluid mixture in the

in-situ condition, we use

$$V_p = 2096\sqrt{\frac{\rho'}{2.6-\rho'}} - 3.7T + 4.64P + 1.15\times10^{-2}\times4.12P\times T\sqrt{\frac{1.08}{\rho'}-1} \quad (3.8)$$

where

$$\rho' = \frac{\rho_o}{B_o(1+1\times10^{-3}GOR)}. \quad (3.9)$$

Finally, the bulk modulus K of the fluid mixture expressed in Pa is given by

$$K = 1000\rho V_p^2. \quad (3.10)$$

3.2.3 Easy %Ro

One of the most widely used models for estimating in-situ Ro is the Easy %Ro proposed by [72]. It takes the simple form

$$\%R_o = \exp(-1.6 + 3.7TR) \quad (3.11)$$

where TR is the transformation ratio denoting the fraction of kerogen that has been decomposed during the thermal maturation. Easy %Ro assumes a series of parallel chemical reactions with Arrhenius type rate constants. The rate constants k associated with those reactions are characterized by a single frequency factor, and a predetermined distribution of activation energies shown in Figure 3.1. We note that Easy %Ro is modeled based on open-system pyrolysis experiments, which produce different end-products from the hydrous pyrolysis. We caution a direct transfer of TR derived from hydrous pyrolysis to Easy %Ro without calibrations to specific hydrocarbon generation kinetics.

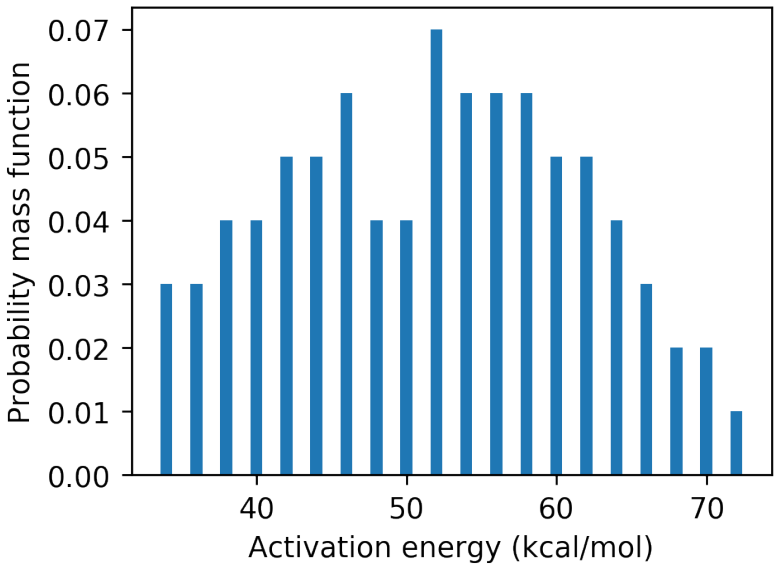

Figure 3.1: Distribution of activation energies specified in Easy %Ro.

3.2.4 Rock physics modeling constrained by hydrous pyrolysis data

Figure 3.2 shows the general workflow of modeling the anisotropic source rock system; the DEM is used twice in estimating the elastic constants. The DEM is first used to estimate the elastic constants of the organic mixture which consists of solid kerogen and hydrocarbons in the liquid phase. The DEM is used again where it mixes the organic part into the inorganic background to compute the overall elastic constants of the source rock system. In modeling the organic mixture, experimental data, including data collected from the hydrous pyrolysis are used to constrain the rock physics models.

Calculating elastic constants for the organic mixture

Figure 3.3 shows the workflow of estimating elastic constants of the organic mixture through the DEM. The organic part is assumed to be either pure solid consisting

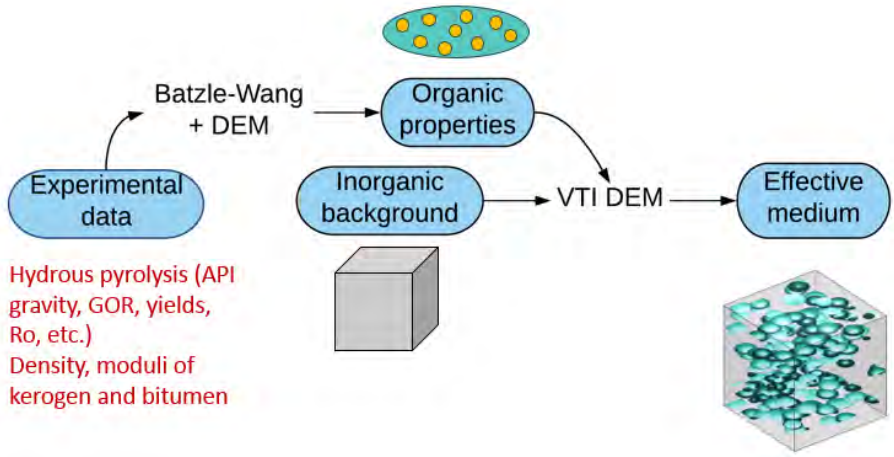

Figure 3.2: Workflow of modeling the source rock system as an effective medium. The DEM is used twice, first in modeling the organic mixture, second in modeling the source rock system. Experimental data are used to constrain inputs when modeling the organic mixture.

of kerogen and bitumen in the immature stage, or a mixture of solid and fluid in the maturing stage, where the liquid comes from the generated hydrocarbons. Because numerous SEM images have revealed bubble-like hydrocarbon-filled nanopores dispersed inside the kerogen, the fluid pockets generated during the thermal maturation are treated as spherical inclusions in our modeling workflow. Those inclusions are added to the solid organic background through the DEM. We use experimental data, especially hydrous pyrolysis data to constrain the inputs used in the DEM and in the Batzle-Wang's relation. Specifically, the elastic properties of the solid organics are determined from laboratory measurements based on [43, 83, 26]; inputs into the Batzle-Wang's relation (e.g. API gravity, GOR, gas gravity, etc.), which we use to estimate the elastic properties of the fluid phase, are collected from, or calculated based on the hydrous pyrolysis experiments.

Additionally, volume fractions of solids and fluids within the organic mixture, which vary with the thermal maturity level, can also be estimated from hydrous

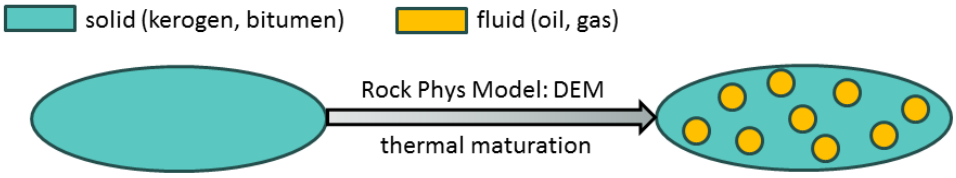

Figure 3.3: Recipes for modeling organic mixtures. As the thermal maturation takes place inside the kerogen, the kerogen transforms into solid bitumen, and oil- and gas-bearing fluids. The fluid pockets have bubble-like shapes, which are modeled as spherical inclusions inside the solid organic background. The DEM scheme is used for estimating the elastic constants of the organic mixtures.

pyrolysis experiments, and mapped to various maturation stages. The underlying assumption here is a correspondence between the products produced from the hydrous pyrolysis and in-situ conditions at any thermal maturation stage. This assumption has been tested and endorsed by [48]. Table 3.1 shows yields of the kerogen, bitumen, oil, and total gas collected by [70] from a set of hydrous pyrolysis experiments. Figure 3.4 shows those yields plotted as a function of Ro, and a calculated total yield shown in the black curve. We observe that the black curve is essentially flat across different maturity levels, which suggests that the mass of the organic matter is conserved. We approximate the volume fraction of the fluids within the organic mixture to be the ratio of the yield of fluids (sum of green and red curves) to the total yield (black curve). We note that by equating the volume fractions to the weight fractions, we omit the effect of density contrast between the solid and fluid parts, which may become more pronounced at late maturity levels, during which the solid becomes denser, while lighter hydrocarbons are formed. Within the oil window under consideration (Ro below 1.2%), the density contrast should not be problematic. Figure 3.5 shows the calculated volume fraction of fluids in the organic mixture based on the hydrous pyrolysis data. The data show a consistently increasing trend in the volume fraction of fluids from almost 0 in the immature stage to over 0.6 at an Ro of 1.2%. We further fit a sigmoid curve through the data points, and obtain a relationship between the

Table 3.1: Product yields in mg/g TOC_o of kerogen, bitumen, oil and gas and transformation ratio (TR) obtained from each hydrous pyrolysis experiment from [70] Table 3.

T (°C)	kerogen	bitumen	expelled oil	total gas	TR (%)	Ro (%)
280	690.33	407.60	6.65	40.92	1.6	0.44
300	452.63	534.74	25.94	49.99	5.0	0.47
310	271.87	724.24	58.61	63.39	10.1	0.52
320	218.73	844.84	122.14	76.41	19.7	0.58
325	184.24	816.58	171.17	87.67	26.8	0.71
330	205.67	768.14	229.53	104.38	35.6	0.75
340	260.84	492.31	355.87	123.94	54.2	0.81
345	296.88	409.90	467.26	140.16	70.5	0.83
350	275.02	298.92	521.49	135.92	78.2	0.86
355	282.69	265.28	543.34	146.20	81.8	1.08
360	324.54	187.87	662.17	165.78	100.0	1.08
365	320.80	148.70	632.17	184.75	NaN	1.13

volume fraction of fluids and the thermal maturity indicator, Ro. The fitted curve writes

$$\frac{v_{fluid}}{v_{inclusion}} = \frac{0.70}{1 + \exp\left(-(8.72R_o - 6.61)\right)} \tag{3.12}$$

where v_{fluid} is the volume of the fluid phase, and $v_{inclusion}$ is the volume of the organic mixtures, or equivalently the inclusions. Once the relative volume fractions are determined within the organic mixtures, we use the DEM scheme to calculate the effective elastic constants of the organic mixture.

Calculating elastic constants for the source rock system

After we calculate the elastic properties for the organic mixture, the organic mixtures are then treated as inclusions, and added to the inorganic background to form an effective medium for the source rock system as shown in Figure 3.6. Depending on the nature of the source rock, the background can be intrinsically isotropic or

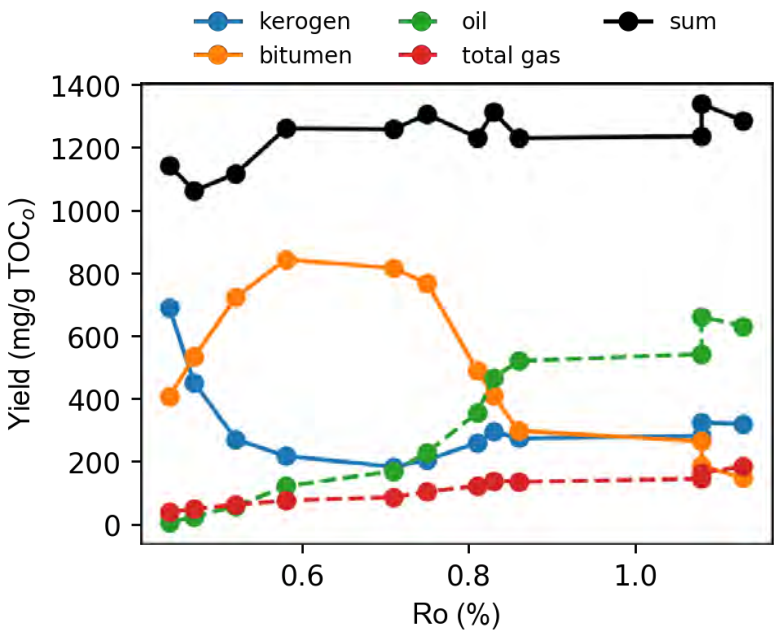

Figure 3.4: Yields of kerogen (blue), oil (green), bitumen (orange) and total gas (red), as well as the calculated total yield (black) plotted as a function of the vitrinite reflectance based on [70] and Table 3.1.

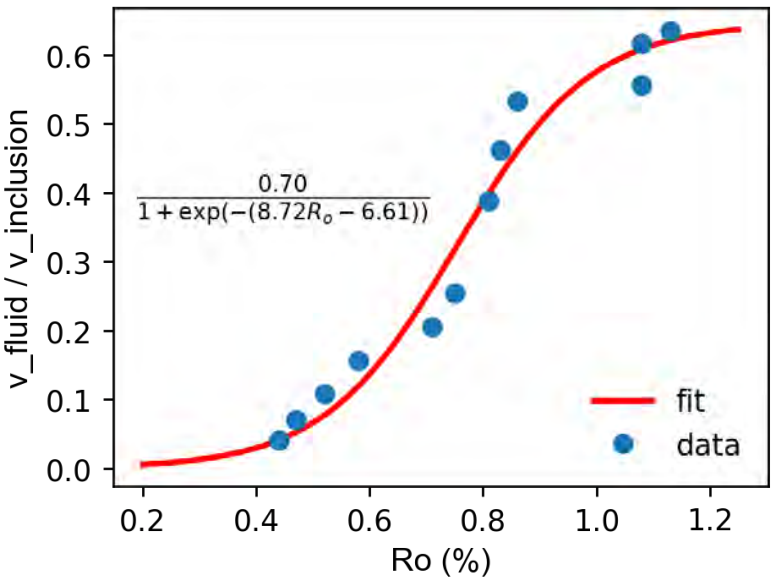

Figure 3.5: Ratios of volume fractions of fluids to organic inclusions as functions of the vitrinite reflectance. The data points are calculated based on [70]'s hydrous pyrolysis measurements; the red curve is a fitted curve assuming a sigmoid function form.

anisotropic; a typical anisotropic scenario is a VTI shale background. In the "Results and discussion" section, we will first analyze the results based on an isotropic inorganic background with a P-wave modulus of 30 GPa and an S-wave modulus of 10 GPa to study the maturation-induced anisotropy. Later, we will analyze results based on a VTI inorganic background, where the five independent elastic stiffness components are $c_{11} = 34.3$ GPa, $c_{33} = 22.7$ GPa, $c_{44} = 5.4$ GPa, $c_{66} = 10.6$ GPa, and $c_{13} = 10.7$ GPa taken from [39]. Many SEM images reveal oblate spheroidal shapes in kerogen lenses with the axis of symmetry aligned with the normal of the bedding planes. Therefore, we experiment with three aspect ratios, namely 0.05, 0.1 and 0.2, for the spheroidal organics-filled inclusions perpendicular to the 3 (z)-direction. The organics-filled inclusions assume to take a total volume fraction ϕ of 10% of the effective medium, which in reality can be estimated from the total organic carbon in the immature state (TOC_o) and the kerogen type. The inclusions are incrementally added into the

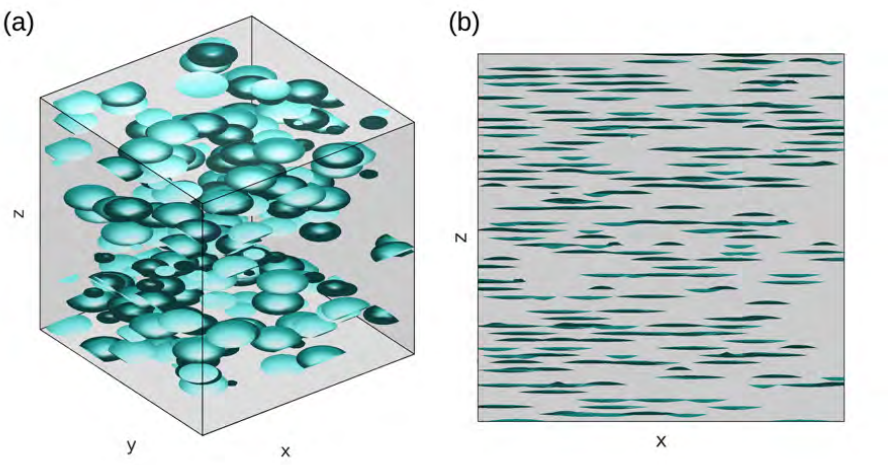

Figure 3.6: Schematics of a 3D representation (a) and a 2D side-view (b) of a source rock system. Oblate cyan spheroids symmetric about the z-direction denote the organics-filled inclusions. The gray background denotes the inorganic background matrix.

inorganic background up to $v = \phi$ through the anisotropic DEM scheme given by Eqn.(3.1).

3.3 Results and discussion

3.3.1 Modeling geological context

Figure 3.7 demonstrates the use of Easy-%Ro [72] to predict the thermal maturity of the source rock as a function of the geologic time under a constant sedimentation rate of 100 m/m.y., a constant heating rate of 0.025 °C/m, and a surface temperature of 0 °C. The TR for both the vitrinite and oil generation reactions are calculated assuming the Arrhenius type chemical kinetics. Specifically, a single preexponential factor A of $1 \times 10^{14}\,\mathrm{s}^{-1}$, and a distribution of activation energies are used for the vitrinite generation [72]; a single pair of preexponential factor and activation energy

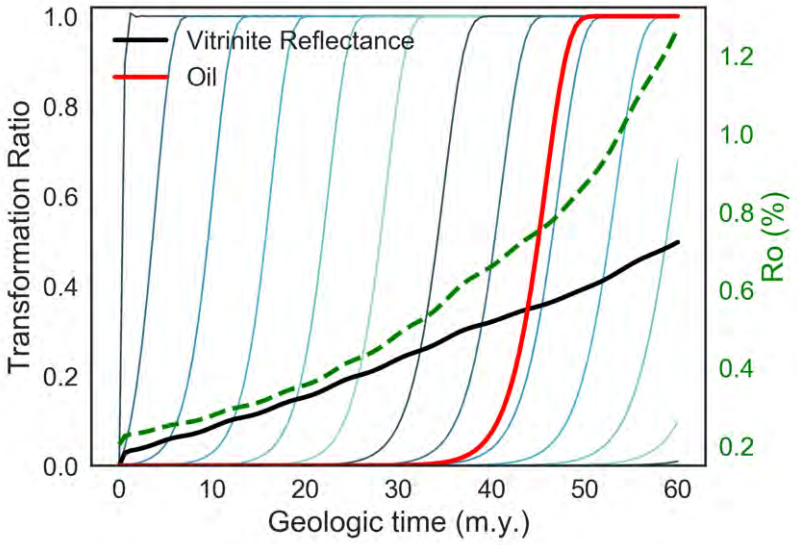

Figure 3.7: Evolution of transformation ratios of the vitrinite reflectance (black) and oil (red) over the geologic time assuming constant sedimentation rate of 100 m/m.y., and a constant heating rate of 0.025 °C/m. The calculated vitrinite reflectance using Easy %Ro [72] is juxtaposed in the dashed green.

same as Chapter 2, which is $A = 5 \times 10^{13}\,\mathrm{s}^{-1}$ and $E = 49$ kcal/mol, is used for the oil generation. From the red curve, we observe that the peak oil window lies between 40-50 m.y., which corresponds to an Ro around 0.6-0.8% shown by the dashed green curve, a typical range for the onset of the oil window. Meanwhile, the vitrinite generation shows a more steady increase over the geologic time. This is due to the fact that the vitrinite generation combines a series of reactions, all of which have different activation energies. Each single reaction is represented by the curves shown in blue to cyan in Figure 3.7. The Easy-%Ro formulation provides a pathway to connect experimental data with the geologic setting.

3.3.2 Elastic properties of the organic part

Figure 3.8 plots the P-wave modulus M and shear modulus G of the organic mixture calculated from the DEM as a function of the thermal maturity level Ro. We used a

bulk modulus of 7 GPa, and shear modulus of 2.33 GPa for the solid organic part. The bulk modulus of the oil was estimated 0.67 GPa based on the Batzle-Wangs relation; the inputs to the Batzle-Wang's relation were based on the mean values of parameters collected from [70]'s hydrous pyrolysis experiments. The resulting P-wave and S-wave moduli of the organic mixture reveal a significant reduction in the oil window, where Ro is between 0.6% and 0.8%.

Figure 3.9 shows the sensitivity analysis that addresses the uncertainties in the elastic property measurements inside the organic mixture. The left plot of Figure 3.9 shows the error bars for the case where the bulk modulus of the oil is either 50% less or greater than the original value. The motivation of this exercise is that we observed the API gravity, GOR, and other fluid properties change as a function of the thermal maturity level from the hydrous pyrolysis experiments; we would like to see if those changes have a significant impact or not on the moduli of the organic mixture. From the plot we see that the variation in the fluid properties only has a limited amount of effect in determining the P-wave modulus of the organic mixture; this is expected because the S-wave modulus is zero for the fluid regardless of the fluid properties.

The right plot of Figure 3.9 shows the error bars where the solid organic part has the bulk and shear moduli either 20% less or greater than the original values. Now the error bars are much wider, especially at earlier maturation stages where the solids dominate in the organic mixture. Also we note that the uncertainty range in the solid part is 20% around the original value in this case, contrasting to 50% in the previous case. This comparison clearly indicates that good measurements of the solid properties are more critical than those of the fluids. Unfortunately, the changes in the bulk and shear moduli for the kerogen bitumen over the thermal maturation are not usually taken into consideration. This could have greatly increased the uncertainties associated with the elastic property estimates for the organic mixture.

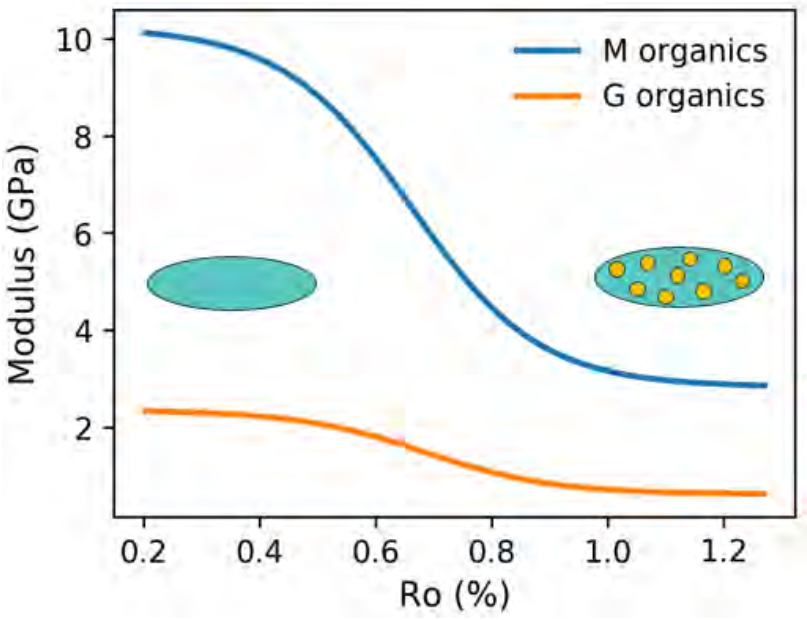

Figure 3.8: Calculated P- and S-wave moduli of the organic mixture plotted as a function of the vitrinite reflectance using DEM. The solid organic part assumes a bulk modulus of 7 GPa and a shear modulus of 2.33 GPa. The generated hydrocarbons have a bulk modulus of 0.67 GPa determined from the Batzle-Wang's relation.

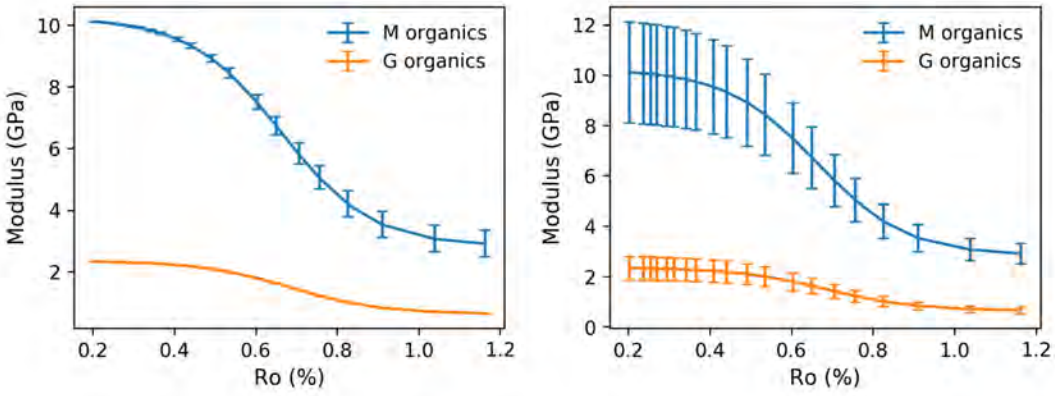

Figure 3.9: Sensitivity analysis of the P- and S-wave moduli of the organic mixture. Left: the bulk modulus of the fluid phase is 50% less or greater than the original value, which is 0.67 GPa. Right: the bulk and shear moduli of the solid phase is 20% less or greater than the original values, which are 7 GPa and 2.33 GPa, respectively.

3.3.3 Elastic properties of the source rock system for an isotropic inorganic background

The evolution of the elastic properties of the source rock for an isotropic inorganic background is shown in Figure 3.10. The left plot shows the evolution of the P-wave moduli over the maturation process, and right plot shows the case for the S-wave moduli. We observe that although the inorganic background matrix is defined as isotropic, the addition of the aligned flat inclusions makes the source rock VTI. Throughout the maturation process, $c_{33}, c_{44}/c_{55}$ have more pronounced reductions, because they have either the particle motion or the wave propagation direction parallel to the axis of the rotational symmetry of the inclusions. This alignment makes them more sensitive to elastic property changes in the organic mixture. Still, c_{11}/c_{22} and c_{66} are decreased by a small amount as the rock becomes more mature. Also, inclusions with lower aspect ratios result in more reduction in the stiffness, which is expected because the crack-like inclusions are more compliant, leading to more significant softening of the rock.

Figure 3.11 shows the evolution of the anisotropy parameters of the source rock with an isotropic inorganic background. One obvious thing to observe is that the anisotropy is enhanced during the thermal maturation. In both the ϵ and γ parameters, thinner inclusions (lower aspect ratios) result in more significant increase of anisotropy as the rock becomes more mature, but interestingly not in the δ parameter. We speculate that this is mainly due to the less obvious physical meaning of the δ parameter. From Figures 3.10 and 3.11, we find that the most rapid decrease in the elastic stiffness and the the most rapid increase in the anisotropy parameters occur mostly between an Ro of 0.6% and 0.8%, corresponding to the major oil generation time frame. The conversion from solid to liquid results in quite significant change in the overall source rock elastic properties. As a result, the thermal maturation can effectively soften the

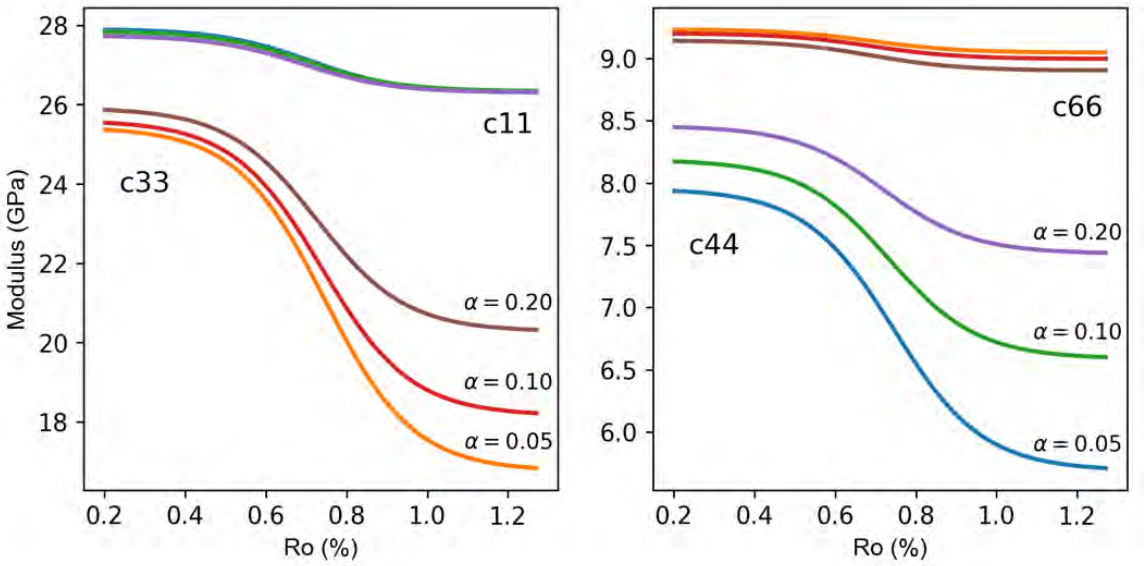

Figure 3.10: Evolution of the elastic stiffness tensor components of the source rock system over the thermal maturation process. P-wave (left) and S-wave (right) moduli are plotted against the vitrinite reflectance. Organic mixtures have a total volume fraction of 10% with aspect ratios 0.05, 0.1 or 0.2.

source rock, and enhance its anisotropy.

Finally, we plotted the V_p/V_s ratio as functions of the P-wave velocity and Ro in Figure 3.12. We used c_{33} to calculate V_p, and c_{44} or equivalently c_{55} to calculate V_s because those are the common ones measured in the sonic logs. To simplify the assumption we used a constant density of 2200 kg/m^3 for the source rock, which may not be accurate because the density may vary with the thermal maturity level as well. From the left plot, we observe an almost linear increase in the V_p/V_s ratio as a function of the P-wave velocity, and higher V_p/V_s ratios in thinner inclusions. From the right plot, we observe a nonlinear decrease in the V_p/V_s ratio as the rock matures, where the rate of the decrease is comparable to the rate at which the components in the source rock elastic stiffness tensor decrease.

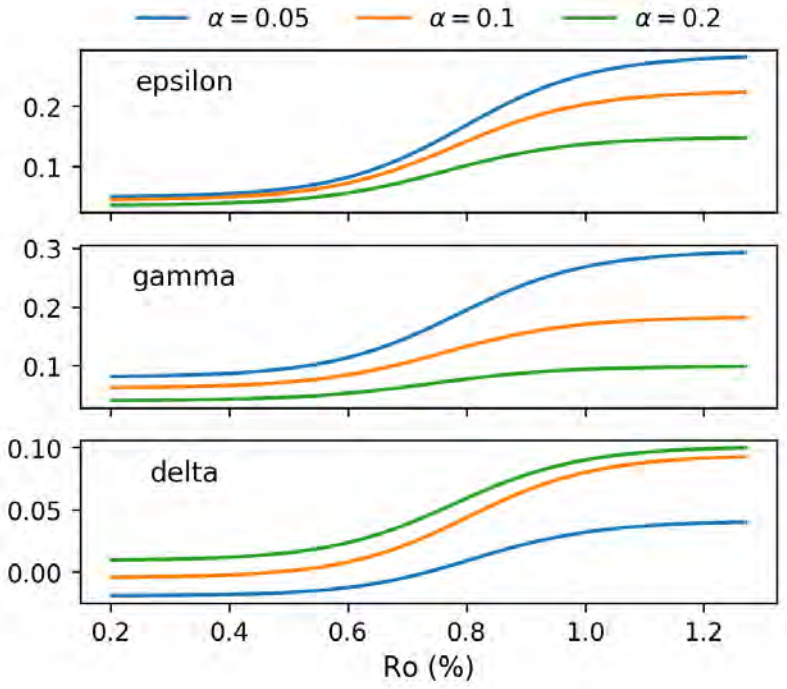

Figure 3.11: Evolution of the Thomsen parameters ϵ, γ, and δ of the source rock system over the thermal maturation process. Organic mixtures have a total volume fraction of 10% with aspect ratios 0.05, 0.1 or 0.2.

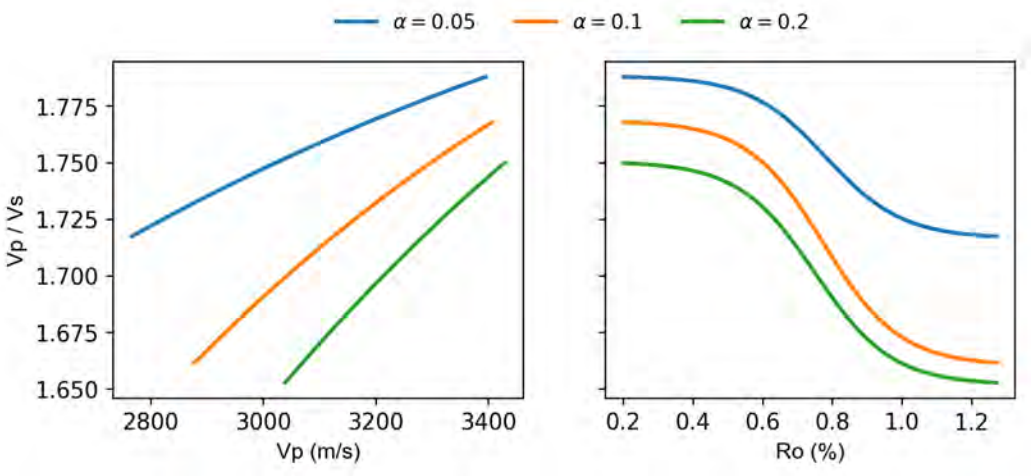

Figure 3.12: Evolution of the V_p/V_s ratio of the source rock as functions of the c_{33} derived P-wave velocity (left) and the vitrinite reflectance (right). A constant density equal to 2200 kg/m^3 was assigned to the source rock. Organic mixtures have a total volume fraction of 10% with aspect ratios 0.05, 0.1 or 0.2.

3.3.4 Elastic properties of the source rock system for a VTI inorganic background

Figures 3.13-3.15 show the evolution of the elastic stiffness, anisotropy parameters and V_p/V_s ratio of the source rock for a VTI inorganic background. Compared to the isotropic case, we observe that both of them follow fairly similar trends throughout the maturation process, although the starting values are different due to the initial conditions. As a result, the conclusions we drew from the isotropic case can be readily extended to the VTI scenario.

3.4 Summary

In this chapter, we introduced an improved rock physics modeling workflow using the effective medium theory to quantify the source rock elastic property evolution as the source rock matures. The source rock system is divided into an inorganic background

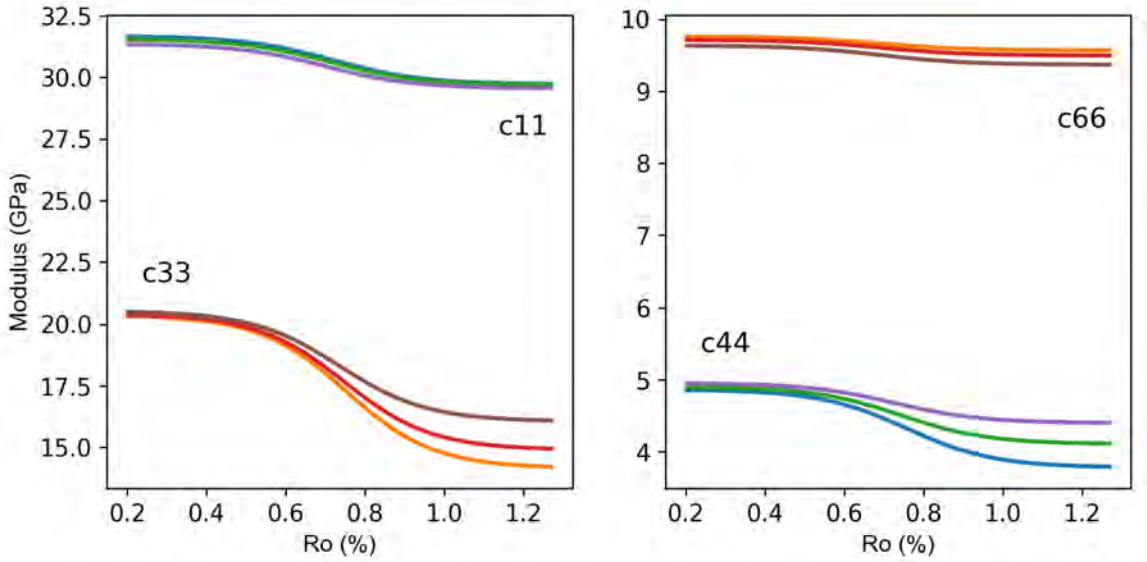

Figure 3.13: Evolution of the elastic stiffness tensor components of the source rock system over the thermal maturation process for a VTI initial inorganic background. P-wave (left) and S-wave (right) moduli are plotted against the vitrinite reflectance. Organic mixtures have a total volume fraction of 10% with aspect ratios 0.05, 0.1 or 0.2 (same color scheme as Figure 3.10).

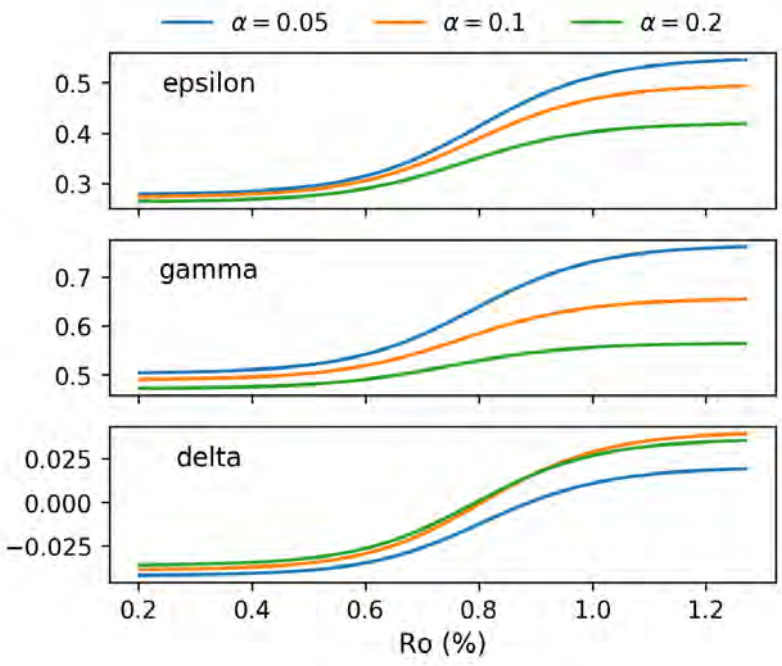

Figure 3.14: Evolution of the Thomsen parameters ϵ, γ, and δ of the source rock system over the thermal maturation process for a VTI initial inorganic background. Organic mixtures have a total volume fraction of 10% with aspect ratios 0.05, 0.1 or 0.2.

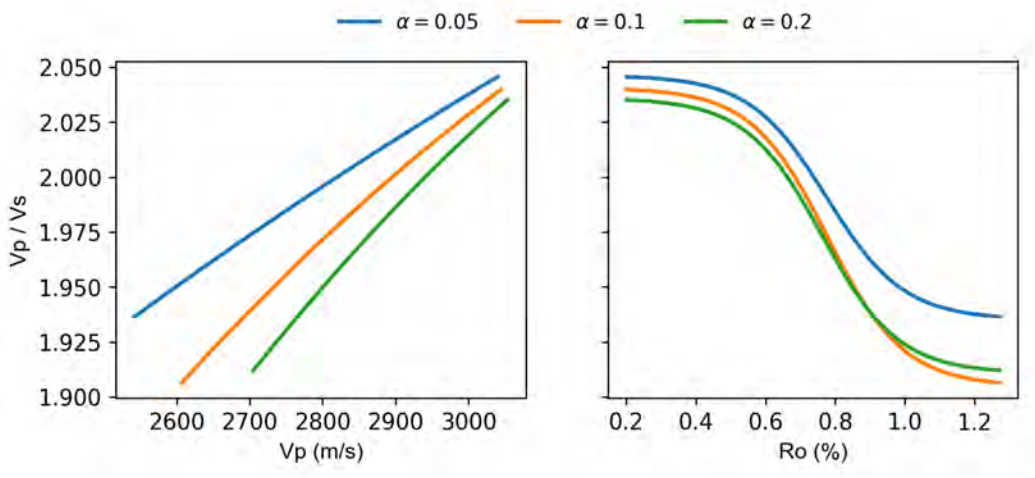

Figure 3.15: Evolution of the V_p/V_s ratio of the source rock as functions of the c_{33} derived P-wave velocity (left) and the vitrinite reflectance (right) for a VTI initial inorganic background. A constant density equal to 2200 kg/m^3 was assigned to the source rock. Organic mixtures have a total volume fraction of 10% with aspect ratios 0.05, 0.1 or 0.2.

matrix containing minerals and water- or air-filled pores, and organics-filled inclusions. The DEM was first used to build an effective medium for the organic part, and then used to build an effective medium for the source rock system. We made use of the experimental data, in particular the data of yields collected from the hydrous pyrolysis experiments to constrain the inputs to the rock physics models. The use of data from hydrous pyrolysis experiments has led to more accurate quantification of the elastic property changes in the organic part during the thermal maturation.

From the effective medium modeling results, we found that the thermal maturation first results in the reductions of the P- and S-wave moduli of the organic mixture; the most pronounced reduction occurs in the oil window corresponding to a vitrinite reflectance range of 0.6-0.8%. The sensitivity analysis showed that good measurements of the elastic properties of the solid organic components (kerogen and bitumen) are more critical than those of the fluids for arriving at accurate elastic constants for the organic mixture. From the source rock system perspective, the thermal maturation

results in enhanced anisotropy and reduced elastic stiffness. The organic inclusions with flatter shapes (lower aspect ratios) result in more significant reduction in the elastic stiffness, and more significant increase in the anisotropy. The elastic stiffness components of the source rock that have either the particle motion or the associated wave propagation direction parallel to the axis of the rotational symmetry of the inclusions are more sensitive to the elastic property changes within the organic part. Finally, the V_p/V_s ratio increases as a function of the P-wave velocity, and decreases as a function of the vitrinite reflectance over the thermal maturation process.

When building the rock physics model for the source rock system, we have made many assumptions. Two of them can be potentially relaxed to reach more comprehensive conclusions. First, in estimating the elastic properties for the organic part, we assumed that the elastic moduli of the solid is constant throughout the thermal maturation. In fact, many experimental data [83, 26] reveal that the bitumen would undergo significant softening during the maturation, making the solid part softer as the rock matures. Because the sensitivity analysis has shown the importance of good elastic measurements of the solid part, the consideration of bitumen softening would certainly lead to better estimation of the organic part elastic properties. Second, in estimating the V_p/V_s ratio of the source rock during the thermal maturation, we have made the assumption that the density of the source rock remains the same. In fact, there is experimental evidence that shows that the density is also strongly affected by the the thermal maturity, especially the organic part [27]. By considering the density effect, the V_p/V_s ratio may result in different trends.

Chapter 4

Seismic facies classification by deep learning

4.1 Introduction

In this chapter, we transition to a different topic, where we introduce a new deep learning based method to classify seismic facies from 3D seismic data. The deep learning based method is a 3D convolutional neural network (CNN) framework. This approach proves to be very promising in making geologically reasonable and consistent predictions of seismic facies.

4.1.1 Motivation

The increasing availability of 3D seismic data demands a workflow for automatic seismic facies classification. Traditionally, the seismic facies interpretation and classification are made by geoscientists. In addition to the tremendous amount of time involved in classifying 3D seismic volumes, the quality of the results is often less controlled due to the variation in geoscientists experiences. A CNN based procedure that automatically

learns and extracts useful features from 3D seismic volumes, and consequently makes seismic facies classification can significantly reduce the human labor and uncertainties, thereby accelerating decision-making time.

4.1.2 Literature review

Deep learning has gained great attentions in the oil and gas industry (Tian (2018) [74], Tian and Horne (2019) [75]). In particular, a few deep learning architectures have shown promising results when applied to geophysical problems. LeCun et al. (1998) [47]'s LeNet-5 CNN architecture can be readily extended and applied to analyzing seismic volumes. Long et al. (2015) [51]'s fully convolutional network (FCN) that builds upon the CNN, and incorporates an encoder-decoder structure, gains attentions in many applications involving seismic inversion and interpretation. A variant of the FCN, the UNet (Ronneberger et al., 2015 [66]), has been widely explored in salt detection problems. Finally, the generative adversarial network (GAN) (Goodfellow et al., 2014 [31]) is an emerging technology that enables generating more training data by training two competing networks.

The geophysical application of the above deep learning architectures can be crudely classified into three categories. First, in the application of generating training data, Mosser et al. (2017) [56] pioneered in using GAN to generate 3D porous rock volumes, and achieved permeability estimates comparable to real rocks. Second, to aid the seismic interpretation, Huang et al. (2017) [33] introduced a scalable computing platform for identifying geologic features from seismic attributes; Araya-Polo et al. (2017) [6] demonstrated the use of CNN for extracting faults without seismic processing; Alaudah and AlRegib (2017) [2] showed the use of "weakly labeled data" for mapping faults; Alaudah et al. (2018) [3] applied the FCN to label seismic structures. Third, to tackle the traditional inversion problems such as the velocity model inversion, Das et al. (2018) [23] showed promising results for impedance inversion using 1D CNN,

while Wang et al. (2018) [80] used the FCN to predict 2D velocity models.

There are a few works that are specifically relevant to our objective, which is to extract seismic facies from seismic volume using CNN. In particular, Waldeland and Solberg (2017) [79] presented a binary classification algorithm for salt dome detection by classifying each pixel using its surrounding 3D seismic information. Ildstad and Bormann (2017) [34] extended Waldeland and Solberg (2017) [79]'s strategy by making multi-class seismic facies predictions using similar input data formats and CNN architectures. Our work bases on the "MalenoV" repository and labeled data created by Ildstad and Bormann (2017) [34], and aims to further improve the prediction accuracy and computational speed.

4.1.3 3D seismic dataset

The 3D seismic dataset used in this piece of work comes from a public seismic survey from block F3 located in the North Sea offshore of Netherlands [24]. The 3D seismic data (cube) has a volume of size $651 \times 951 \times 462$ in the inline, cross-line (xline), and time directions, respectively. The bin size for both the inline and xline directions is 25 m, and the spacing along the time direction is 4 ms. This survey covers an area of size approximately 24 km by 16 km. Figure 4.1 shows the inline 339 2D section extracted from the 3D seismic cube, which has a size of 951×462. Ildstad and Bormann (2017) [34] labeled 9 classes (8 seismic facies + 1 background class) on 140,111 pixels from the inline 339 section; the labeled areas pixels are shown in Figure 4.2 by different colors. The 9 seismic facies are: steep dips, salt, low coherency, low amplitude, low amplitude dips, high amplitude, high amplitude continuous, grizzly and background. The training, validation, and test sets were prepared in a way such that each sample is a 3D sub-cube of size $65 \times 65 \times 65$ with the central voxel (pixel) belonging to one of the labeled pixels in the inline 339 section.

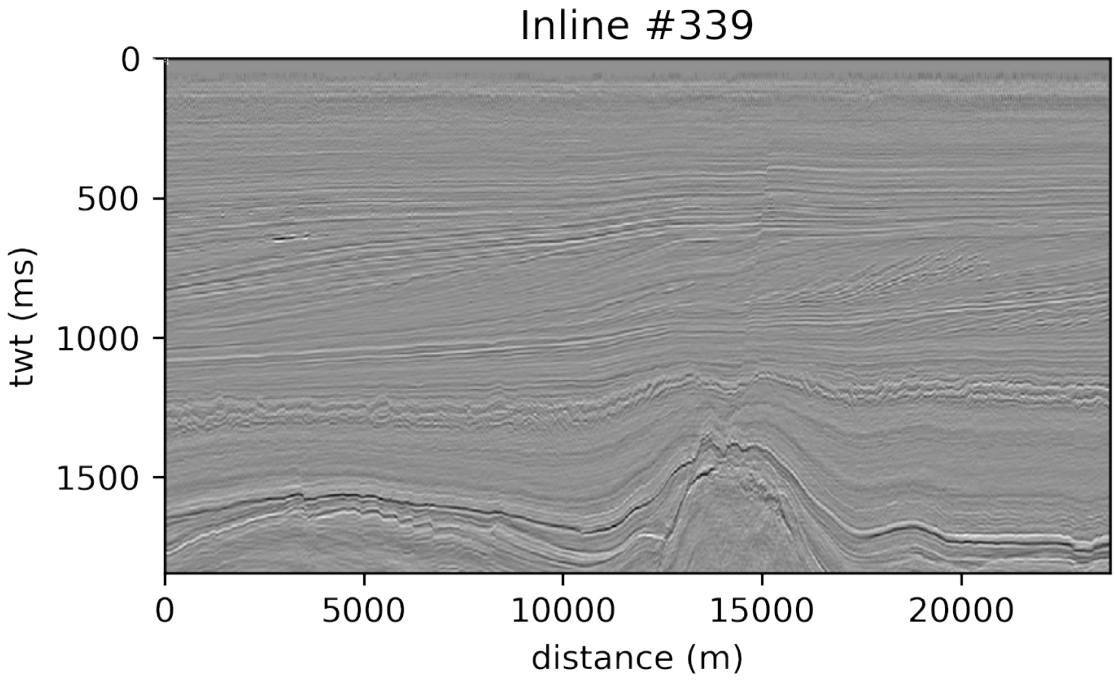

Figure 4.1: Inline 339 section from the Netherlands North Sea offshore F3 block.

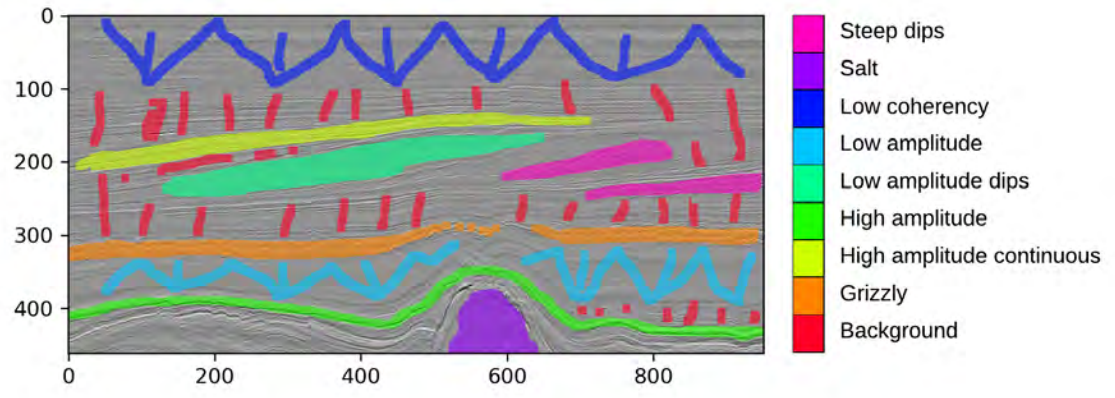

Figure 4.2: Labeled pixels on the inline 339 section.

4.2 Methods

4.2.1 CNN overview

The CNN is the most popular deep learning based method for classifying images. We can first think of CNN as a "black box". We give the black box an input image, and it outputs the probability associated with each pre-defined category for that image, and labels the image based on the highest probability. The CNN is a supervised learning algorithm, which means that it requires labeled training data to help adjust the parameters in the network during training time. To this end, the CNN maintains a scalar value called a loss, and attractively reduces it by performing gradient descent with respect to each adjustable parameter in the "black box" during training time. There are various loss functions, but they all penalize incorrect predictions. If the CNN is designed appropriately, and receives sufficient amount of training data, the parameters inside the "black box" can be optimally tuned at the end of the training time, so that it can output accurate predictions during prediction time.

CNN building blocks

The essential building blocks for any CNN architectures consist of the convolutional layers, nonlinearity function, pooling layers, fully connected (FC) layers and a classifier. A convolutional layer consists of one or multiple filters. Each filter is represented by a high-dimensional tensor, where the weights for all the entries are learned and adjusted during training. The filter size is usually much smaller than the input volume size. The goal of each filter is to learn some generic patterns and their combinations which are best representative for specific labels. The CNN makes use of those learned patterns and features to make predictions. The convolution is in reality a dot product between the weights in the filter and the activated region in the input volume that is is scanning over. Because it is a linear operation, a nonlinearity function, such

as the rectified linear unit, or "ReLu", is frequently added immediately after the convolutional layer to selectively pass information into the next layer. Concretely, the "ReLu" function $f(x)$ is defined as $f(x) = \max(0, x)$ where x is the output from the convolutional layer.

The filter size, channels, strides and zero-paddings

When designing convolutional and pooling layers for the CNN architecture, we need to fine tune the spatial arrangement for each layer by adjusting the filter size f, number of channels, strides s and zero-padding schemes. Specifically, they are defined as:

- The filter size defines the size of the receptive field. When looking at a fixed location, a larger filter takes in more spatial information around that point, but it suffers from maintaining more parameters. In a convolutional layer, a filter takes in information from all the channels from the previous layer, which implies that it must have a dimension equal to the number of channels in the previous layer. During the convolution, the filter performs a dot product with the activated region in the input volume, and outputs a scalar corresponding to a specific entry in the output volume. Note that the channel dimension in the previous layer is contracted during the convolution.

- The number of channels corresponds to the number of filters used in one convolutional layer. Within one layer, all the filters have the same size. While performing dot products, each filter reduces the output dimension by 1 due to the contraction of the channel dimension in the previous layer. The use of multiple filters allows the creation of a new dimension in the output volume with the size equal to the number of filters, or equivalently the number of channels in the current layer.

- The stride is the number of steps each time we slide the filter. A stride of 1

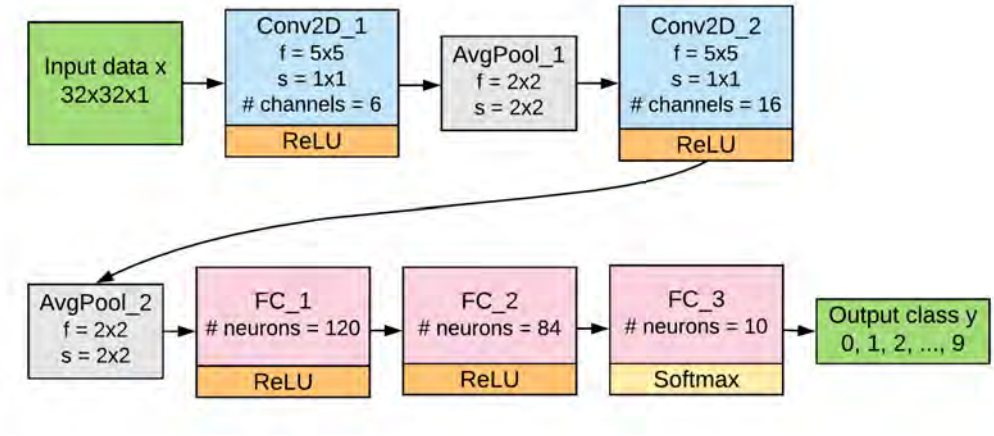

Figure 4.3: The original LeNet-5 2D CNN architecture.

means that we move the filters one pixel at a time. Note that we can use different strides along different dimensions. The output volume size along each dimension is roughly reduced by a factor equal to the stride along the same dimension.

- Zero-padding is frequently used in order to preserve the output volume size. For instance, a black and white image (number of channels = 1) with a size of $W \times H$ becomes $(W-2) \times (H-2)$ after passing through a 2×2 filter with a stride of 1 in each dimension. Often times we would like to keep the original size after the filtering, so we pad zeros around the $(W-2) \times (H-2)$ output to convert it back to $W \times H$.

4.2.2 New CNN design: the modified LeNet-5

LeNet-5 is one the pioneer CNN networks that was designed to detect the ten digits from black and white images. Figure 4.3 shows the original LeNet-5 architecture. Inspired by the LeNet-5, we made major improvement on the CNN architecture on top of [34]'s CNN design. The original CNN architecture, which is shown in Figure 4.4, was fairly crude: three of the five convolutional layers used the same filter design,

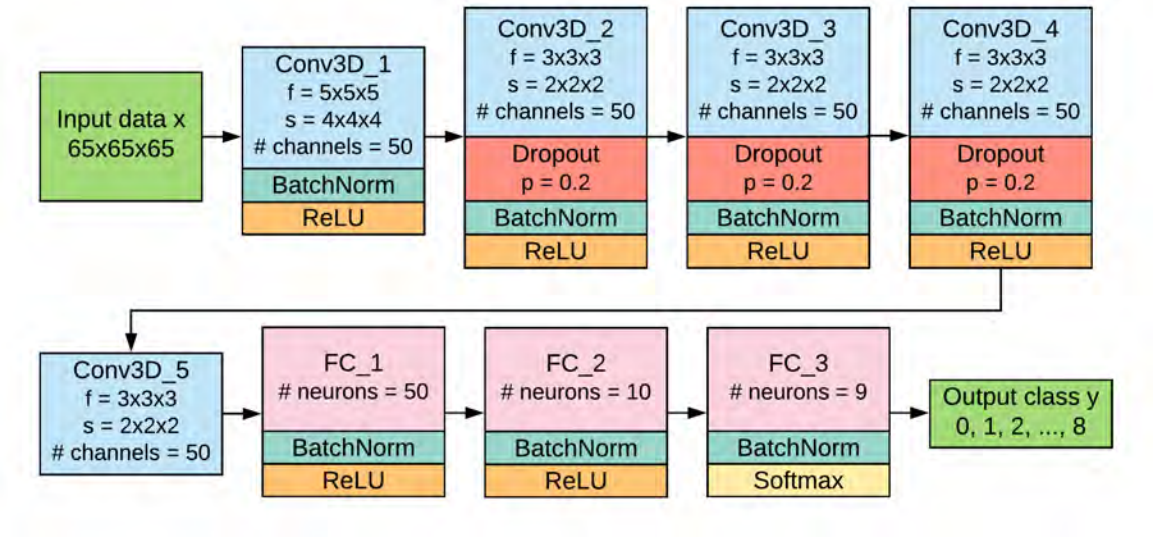

Figure 4.4: The original CNN design in [34].

which is a 50-channel $3 \times 3 \times 3$ filter; no max-pooling layers were included. The new CNN architecture we redesigned, as shown in Figure 4.5, is a variant of the LeNet-5 named "the modified LeNet-5". The new design incorporated the overarching concept that the number of channels of filters should increase while the filter size should decrease as the layers go deeper. Two max-pooling layers were added in order to enhance local features; the dimension of the filter tensors was increased by 1 so that 3D convolution can be performed on the input sub-cubes. The new CNN design demonstrates significant improvement in the loss reduction and training accuracy gains in the early training stage; the results are analyzed in details in the "Results and discussion" section.

4.2.3 Input data preprocessing: sparse sampling

When generating sub-cubes for the input data, we implemented a feature that sparsely samples from the raw seismic cube at a specified step size to preprocess the input data. Initially, the $65 \times 65 \times 65$ sub-cubes were generated by continuously sampling around

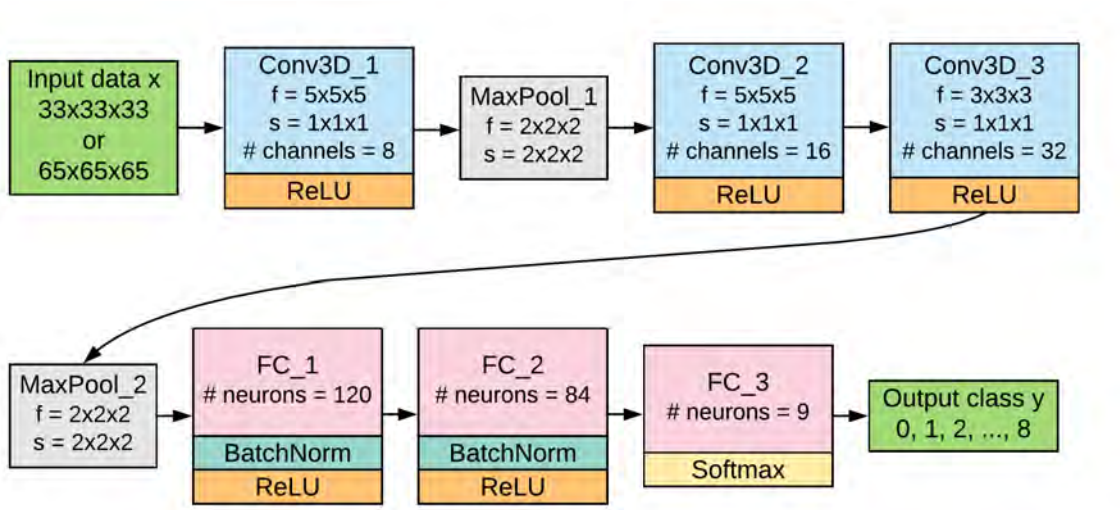

Figure 4.5: The modified LeNet-5 3D CNN architecture.

the labeled central voxels. The sparse sampling scheme improves the computational speed by reducing the sub-cube size. Figure 4.6 shows the comparison between the continuous sampling scheme, and the sparse sampling scheme at a step size of 2 in each dimension, resulting in a sub-cube of size $33 \times 33 \times 33$. The new sub-cube essentially keeps the same receptive field as the old $65 \times 65 \times 65$ sub-cube, but the data size is reduced by a factor of 8. When the input data size is not an issue, the sparse sampling scheme also enables storing more spatial information, potentially improving the prediction accuracy for large-scale features.

4.2.4 Cross-entropy loss

In order to successfully train an effective CNN for the making good predictions, it is essential to select a good loss function and an efficient optimizer. For multi-class prediction problems, the preferred loss function is usually the "cross-entropy" loss. To understand this loss function, it is constructive to first introduce the "softmax" classifier, which assigns scores to each possible class given a data point.

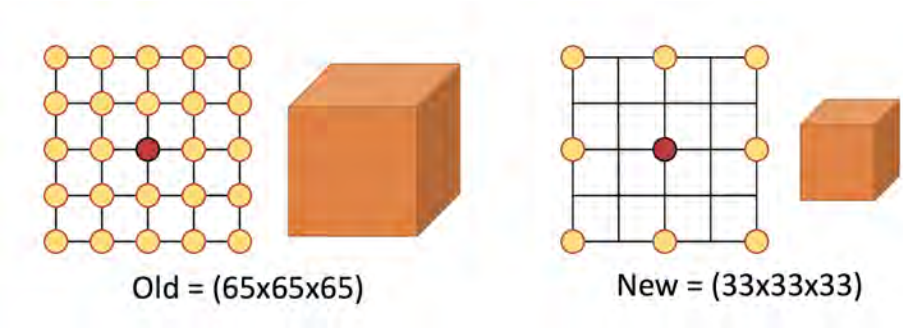

Figure 4.6: Illustrations of sampling schemes. Left: the original continuous sampling scheme and the resulting sub-cube of size $65 \times 65 \times 65$; right: the sparse sampling scheme around the labeled central voxel in red at a step size of 2 along each dimension and the resulting sub-cube of size $33 \times 33 \times 33$.

The softmax function S as defined as

$$S(l_i) = \frac{\exp(l_i)}{\sum_{k=1}^{C} \exp(l_k)} \tag{4.1}$$

where l_i is the "logit" or "score" corresponding to class i, and $S(l_i)$ computes the probability belonging to class i based on the scores. Note that the given a data $\mathbf{x_i}$, the sum of probabilities for all possible classes is equal to 1.

The loss function L_i associated with a particular sample $\mathbf{x_i}$ is defined as

$$L_i = -\sum_{k=1}^{C} y_k \log(S(l_k)) \tag{4.2}$$

where k is summed for all the classes ($C = 9$ in our case). The label y_k is 1 if $\mathbf{x_i}$ belongs to class k, and 0 otherwise. By minimizing Eqn.(4.2), we can maximize the probability $S(l_k)$ when $\mathbf{x_i}$ belongs to class k, whereby minimizing the probabilities for other classes to which $\mathbf{x_i}$ does not belong. This is equivalent to maximizing the probability of having correct predictions.

If we represent the mapping from input data to scores learned by the CNN as f_θ,

we can rewrite Eqn.(4.2) as

$$L_i = -\mathbf{y_i}^T \log\left[S(f_\theta(\mathbf{x_i}))\right] \tag{4.3}$$

where $\mathbf{y_i}$ is represented as a one-hot vector, and f_θ maps the input data $\mathbf{x_i}$ to scores for all the possible classes. Finally, the total loss L for m samples is sum of losses from each term. Namely,

$$L = \sum_{i=1}^{m} L_i = -\sum_{i=1}^{m} \mathbf{y_i}^T \log(S(f_\theta(\mathbf{x_i}))). \tag{4.4}$$

To reduce the loss we can use different gradient descent algorithms to achieve this. One popular choice is the mini-batch stochastic gradient descent (SGD) by using the Adam optimizer.

4.2.5 SGD and Adam optimizer

The SGD is a method that can greatly speed up the parameter updates during training. In each iteration, the SGD only takes in one randomly selected training data from the training set, and updates the parameters according the update rule of the chosen optimizer. The drawback of the SGD is that the learning curves can be rather noisy due to the high variance associated with each individual data point. To addredss this issue, people resort to mini-batches, where during each iteration, 10 to 100 data points randomly selected from the training set are fed into the deep learning network to make parameter updates. Several optimizers have been designed to carry out the mini-batch SGD. In this piece of work, we use the "ADAptive Moment" optimizer, or the "Adam" optimizer introduced by [41]. It is one of the most popular choices in the deep learning community nowadays.

The general update rule for the parameter vector θ in the Adam optimizer is given

by

$$\theta_{t+1} = \theta_t - \frac{\alpha}{\sqrt{\hat{v}_t} + \epsilon}\hat{m}_t \tag{4.5}$$

where $\hat{m}_t$ and $\hat{v}_t$ are bias-corrected first and second moments of the gradient g_t, respectively; ϵ is usually taken to be 10^{-8}, and is used to ensure the stability of this equation; α is the learning rate. The first and second moments represent the mean and the uncentered variance of the gradient g_t, respectively. The bias-corrected estimates are given by

$$\begin{aligned} \hat{m}_t &= \frac{m_t}{1-\beta_1^t} \\ \hat{v}_t &= \frac{v_t}{1-\beta_2^t} \end{aligned} \tag{4.6}$$

where m_t and v_t are the first and second moments without bias-correction. They are incrementally updated according to

$$\begin{aligned} m_t &= \beta_1 m_{t-1} + (1-\beta_1) g_t \\ v_t &= \beta_2 v_{t-1} + (1-\beta_2) g_t^2. \end{aligned} \tag{4.7}$$

Usually, β_1 and β_2 are set to constant values, which are 0.9 and 0.999, respectively, and m_t and v_t are initialized as vectors of 0's. The general idea of the Adam optimizer is that it puts more weight in the gradient descent direction based on moving averages from all the previously seen mini-batches. While it still puts weight on the mini-batch drawn from the current iteration by setting $1-\beta_1$ and $1-\beta_2$, their values are usually very small, which can effectively avoid the variance issue encountered in the traditional SGD method.

To scan over the entire training dataset, we need to send in multiple mini-batches into the network, where the number of mini-batches needed is determined by the total number of training samples and the mini-batch size. A complete pass over the entire

training dataset is called an epoch. Usually, to train a network that identifies complex features using a large amount of data, the network needs to be trained over tens and hundreds of epochs, where each training data is used many times. However, in our application, we found that after one or two epochs, the training accuracy can already achieve very high values, most likely because of the relatively simple seismic facies textures, so we only trained our models for a few epochs in each case.

4.3 Results and discussion

We tested four models using different CNN architectures and parameters. In all the cases, 40,000 training, 10,000 validation and 10,000 test samples were randomly drawn without replacement from the 141,111 labeled data points. Because only a few epochs were trained, a fixed learning rate of 0.001 was used except for the base case, where it was initially set to an adaptive learning rate. We used the cross-entropy loss, and the Adam optimizer to carry out the stochastic gradient descent. The mini-batch size was set to 32 for size $65 \times 65 \times 65$ sub-cubes, and 128 for size $33 \times 33 \times 33$ sub-cubes. Two epochs were trained in each case. All the training and predicting processes were completed on the Stanford CEES GPU cluster using 8 NVIDIA Tesla K80 GPUs.

4.3.1 Model selection and comparison

The training loss and accuracy are plotted as a function of the mini-batch number in Figure 4.7. In the legend, the "base" model refers to the original CNN architecture and parameters used in [34]; the "new" models refer to the modified LeNet-5 architecture shown in Figure 4.5; the "65" and "33" refer to the lengths of each dimension in the sub-cubes; the "1" and "2" refer to the step sizes used in sampling from the raw seismic volume.

As shown in Figure 4.7 (a) and (b), the new CNN design demonstrates significant

improvements in several aspects. First, the new design shows a significant performance improvement in the early training stage: the training loss decreases more quickly, and the training accuracy increases more rapidly within the first few mini-batches. This implies that the new CNN architecture is much more advantageous when the computational power is limited: the training accuracy can achieve more than 0.9 within 100 mini-batches, whereas it needs over 1,000 mini-batches in the base case. Second, the new design suffers from far less noise issues than the original design, where we saw in the blue curves much larger perturbations over the course of training process. We speculate the main reason for the large noise level in the original design is the use of a sub-optimal learning rate. The initial learning rate was probably set too large, making the model very difficult to locate the best gradient descent direction. Because we only trained for two epochs, the power of adaptive learning rate is quite limited.

Figure 4.8 shows the unnormalized confusion matrix for "New-3" based on the 10,000 test data. It is obvious that "New-3" does extremely well on correctly predicting all the nine classes. Although the test dataset, which is randomly drawn from all the labeled data, is imbalanced among different categories, the imbalance did not affect any particular underrepresented classes of "New-3". Therefore, we did not apply any special modification to the loss function to address the imbalance issue.

Table 4.1 compares the performance metrics of the above four models. The "Base" model uses the old CNN design and an adaptive learning rate, and gives a test accuracy of 0.9855 at the end of the second epoch. Although the accuracy is fairly high after two epochs, the early training stage performance, as shown in Figure 4.7, is not satisfactory due to its CNN design and the initial learning rate setup. The "New-1" model, which uses the new CNN design, shows significant improvement in the performance in the early training stage in Figure 4.7, but suffers from a much slower training time due to a bigger CNN architecture. The "New-2" and "New-3" models kept the new CNN design, but used smaller input sub-cubes. The reduction of

the input data size effectively reduces the the training time by more than 50%, and achieves higher computational efficiency. Finally, comparing the original continuous sampling scheme in the "New-2" model with the sparse sampling scheme at a step size of 2 in the "New-3" model, we observe that the sparse sampling scheme results in higher validation and test accuracies because it allows for a deeper receptive field. In summary, the new CNN design in combined with the sparse sampling scheme is the best model for seismic facies classification in the current study.

4.3.2 Validation and application to unlabeled sections

As a verification, we made seismic facies predictions on the entire inline 339 section using the trained "New-3" model. Figure 4.9 shows the comparison between the labeled data and predicted results. We observe very good match between the labels and predictions, verifying a test accuracy of more than 0.99. We further made predictions on two xline 2D sections where labels are not available. Figure 4.10 shows the classified results on xline 450 and 610 sections. The top plots show the raw seismic sections, and the bottom plots show the classified results. We observe good agreement in the seismic facies sequence between the xline 450 and 610 sections; the "salt" facies, which are usually present inside antiforms in nature, were labeled within expected regions in both sections. We conclude that the CNN model is able to generate geologically reasonable and consistent predictions.

4.4 Summary

In this chapter, we introduced an improved 3D CNN framework to classify seismic facies from 3D seismic data. Specifically, we fine-tuned the CNN hyper-parameters, and obtained an optimal network which we called the modified LeNet-5 architecture. We also introduced the "sparse sampling" scheme for pre-processing the input data,

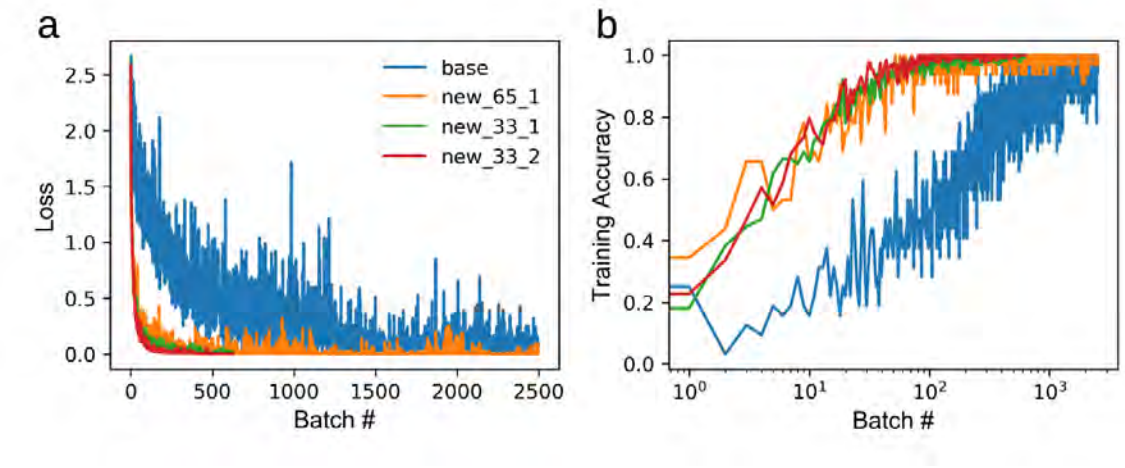

Figure 4.7: Losses (a) and training accuracies (b) plotted against the mini-batch number for four CNN models. The mini-batch number is plotted in the normal scale in (a), and in the logarithmic scale in (b).

which allowed us to reduce the sample size significantly while maintaining a relatively large receptive field. We found that after incorporating these modifications, the improved 3D CNN framework significantly improved the training accuracy in the early training stage. The "New-3" model, which combines the modified LeNet-5 and the sparse sampling scheme, reduces the training time by more than 50%, and achieves a test accuracy of 0.9977, making itself the best CNN model in the current study. Overall, we found that the 3D CNN framework is very promising in making geologically reasonable and consistent predictions for seismic facies based on 3D seismic data.

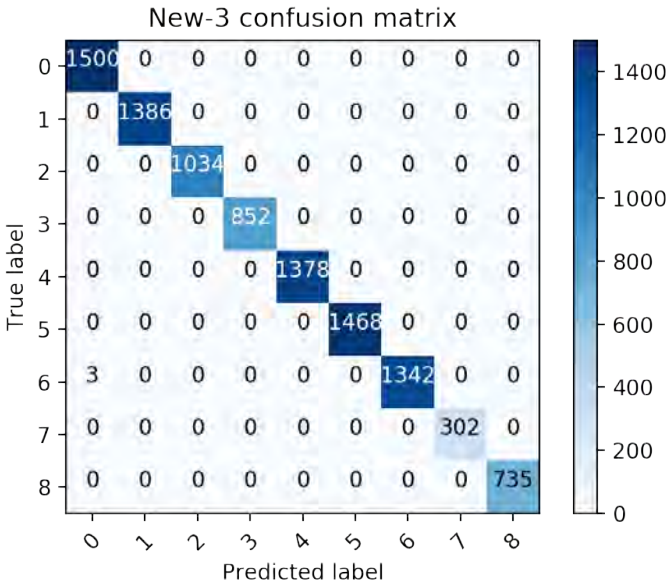

Figure 4.8: Unnormalized confusion matrix for New-3. The numbers 0-8 correspond to the background, grizzly, high amplitude continuous, high amplitude, low amplitude dips, low amplitude, low coherency, salt and steep dips, respectively.

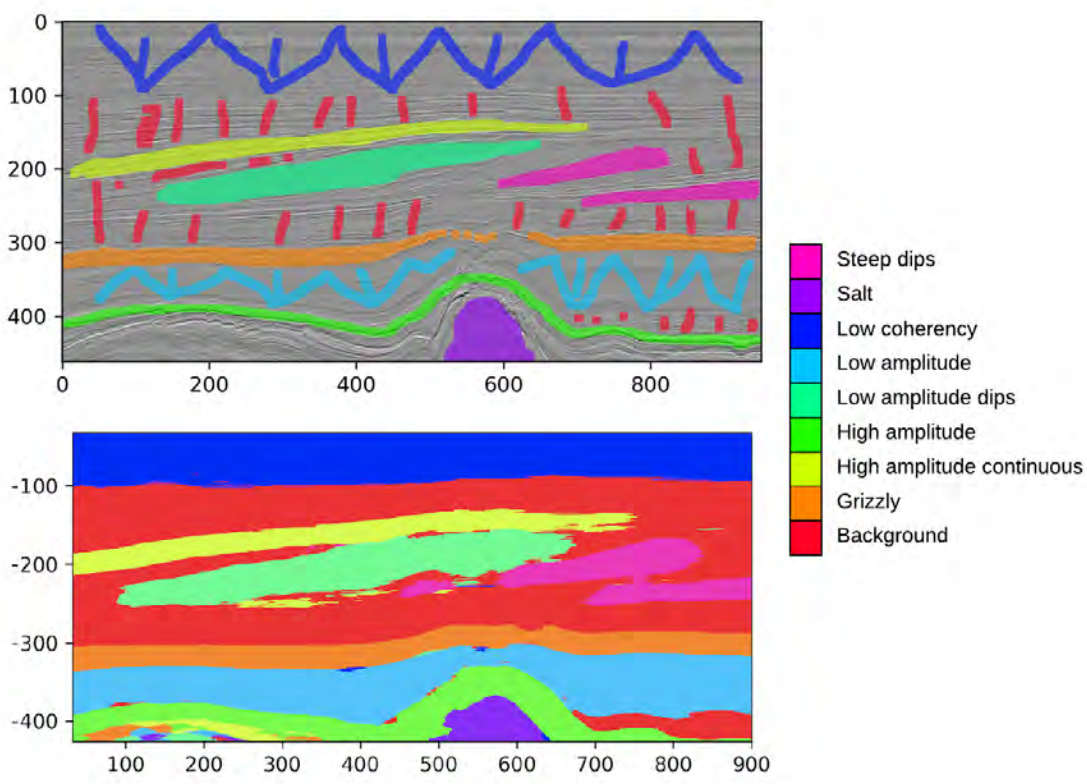

Figure 4.9: Labeled data (top) and predicted results (bottom) on the same inline 339 2D section. The "New-3" model was used for predictions.

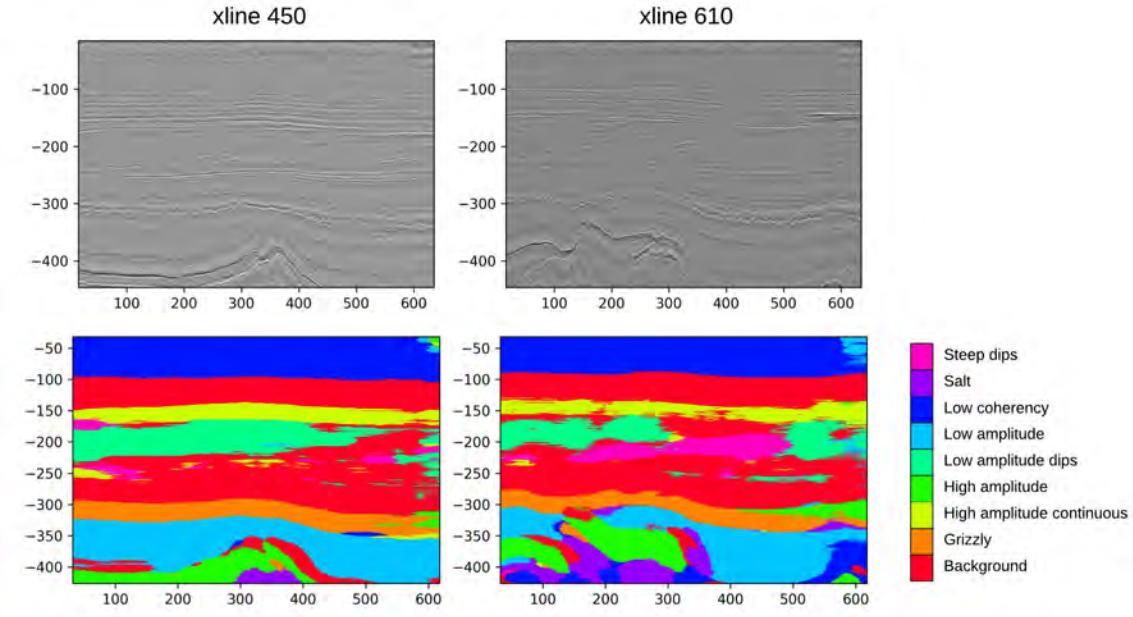

Figure 4.10: Raw seismic data (top) and prediction results (bottom) using the New-3 model on xline 450 (left) and xline 610 (right) seismic sections.

Table 4.1: Performance metrics of four CNN models. New 3 was considered the best model because of its high accuracies and computational efficiency.

Model	Sub-cube size	Step size	Mini-batch size	# of para.	Running time	Train'g acc.	Val. acc.	Test acc.
Base	65	1	32	297,697	7min16s	0.9736	0.9857	0.9855
New-1	65	1	32	8,478,817	29min28s	0.9974	0.9854	0.9853
New-2	33	1	128	522,337	167s	0.9959	0.9488	0.9455
New-3	33	2	128	522,337	187s	0.9991	0.9993	0.9997

Chapter 5

Conclusions and future work

In Chapter 1, we defined essential terminologies used in describing the source rock system, and introduced the thermal maturation process and primary migration concepts which are our main research targets in Chapters 2 and 3. We also revisited the wave propagation fundamentals and elastic anisotropy definitions. A literature review was followed; it covered earlier works on both experimental studies of source rocks as well as various modeling techniques used in studying the effect of the source rock thermal maturation.

In Chapter 2, we presented a model that predicts the microcrack growth and pore pressure changes during the kerogen thermal maturation in organic-rich shales. This model is primarily based on elasticity and LEFM. By running the simulation under laboratory conditions, we obtained similar fracture surface areas to those measured by Kobchenko et al. (2014) [42]. Secondary porosity generated by crack opening is significant under laboratory conditions: the induced crack volume can accommodate several hundred times the initial pore volume. In contrast, under geological conditions, no significant secondary porosity is generated through crack opening. If the kerogen-to-hydrocarbon density ratio is high enough, overpressure can be built up more quickly,

and microcracks can propagate at earlier maturation stages. However, the extent of propagation and resulting apertures are much smaller than those generated under laboratory settings because of the overburden effect. Parametric studies showed that the volume expansion parameter, initial pore size, and fracture toughness of the shale matrix are all major roles in determining the final microcrack sizes and pore pressures to varying degrees. The comparison between laboratory and geological conditions showed that the source rock system behaves fundamentally differently in those two settings; extrapolation from laboratory to geological settings must be treated with care.

In Chapter 3, we improved a rock physics modeling workflow using the effective medium theory to quantify the source rock elastic property evolution as the source rock matures. The source rock system is divided into an inorganic background matrix containing minerals and water- or air-filled pores, and organics-filled inclusions. The DEM was first used to build an effective medium for the organic part, and then was used to build an effective medium for the source rock system. We made use of the experimental data, in particular the data of yields collected from the hydrous pyrolysis experiments to constrain the inputs to the rock physics models. The use of data from hydrous pyrolysis experiments has led to more accurate quantification of the elastic property changes in the organic part during the thermal maturation.

From the effective medium modeling results, we found that the thermal maturation first results in the reduction of the P- and S-wave moduli of the organic mixture; the most pronounced reduction occurs in the oil window corresponding to a vitrinite reflectance range of 0.6-0.8%. The sensitivity analysis further showed that good measurements of the elastic properties of the solid organic components (kerogen and bitumen) are more critical than those of the fluids for achieving accurate elastic constant predictions for the organic mixture. From the source rock system perspective, the thermal maturation results in enhanced anisotropy and reduced elastic stiffness. The

organic inclusions with flatter shapes (lower aspect ratios) result in more significant reduction in the elastic stiffness, and more significant increase in the anisotropy. The elastic stiffness components of the source rock that have either the particle motion or the associated wave propagation direction parallel to the axis of the rotational symmetry of the inclusions are more sensitive to the elastic property changes within the organic part. Finally, the V_p/V_s ratio increases as a function of the P-wave velocity, and decreases as a function of the vitrinite reflectance over the thermal maturation process.

In Chapter 4, we introduced an improved 3D CNN framework to classify seismic facies from 3D seismic data. By fine-tuning the CNN hyper-parameters based off the "MalenoV" repository [34], we obtained a better network that is called the modified LeNet-5 architecture. We also implemented the "sparse sampling" capability for pre-processing the input data, which allowed us to reduce the sample size significantly while maintaining a relatively large receptive field. We found that after incorporating these modifications, the improved 3D CNN framework significantly improved the training accuracy in the early training stage. The combined use of the modified LeNet-5 and the sparse sampling scheme reduced the training time by more than 50%, and achieved a test accuracy of 0.9977, making itself the best CNN model in the current study. Overall, we found that the 3D CNN framework is very promising in making geologically reasonable and consistent predictions for seismic facies based on 3D seismic data.

5.1 Future work

Regarding the directions for the future work, here I'm listing a few that can potentially make the source rock modeling more comprehensive:

- In modeling the microcrack associated with the kerogen thermal maturation, the shale matrix is assumed to be impermeable throughout the whole process. If permeability is present, we would expect the pore pressure to decrease over time, and eventually balance with the hydrostatic pore pressure. To maintain the crack opening after the pore pressure drop associated with fluid flow, inelastic deformation in the shale matrix must occur. This would need more comprehensive modeling of the mechanical evolution of host rocks during the kerogen thermal maturation. The impermeable assumption of our source rock system implies that our model primarily applies to the early hydrocarbon generation and retention stages before any expulsion takes place. The formation of microcracks connects isolated microscale hydrocarbon pockets, providing pathways for the primary migration in later stages.

- When building the rock physics model for the source rock system, two assumptions can be potentially relaxed to take more factors into consideration. First, in estimating the elastic properties for the organic part, we assumed that the elastic moduli of the solid is constant throughout the thermal maturation. In fact, many experimental data [83, 26] reveal that the bitumen would undergo significant softening during the maturation, making the solid part softer as the rock matures. Because the sensitivity analysis has shown the importance of good elastic measurements of the solid part, the consideration of bitumen softening would certainly lead to better estimation of the organic part elastic properties. Second, in estimating the V_p/V_s ratio of the source rock during the thermal maturation, we have made the assumption that the density of the source rock remains the same. In fact, there is experimental evidence that the density of the organic part shows a strong dependence on the thermal maturity [27]. By considering the density effect, the V_p/V_s ratio may result in different trends.

- The 3D CNN framework shows a promising starting point of leveraging deep learning for automatic seismic facies extraction. This workflow can be reliably applied to more 3D seismic volumes if we have a larger training dataset, encompassing labels on slices cut from all the three directions. Additionally, different seismic volumes have different signal-to-noise ratios, which lead to different representations for the same seismic facies. By mixing labels drawn from different seismic volumes, the trained network may have a more robust performance in the testing time.

Appendix A

Proof of crack propagation stability

Here I offer a sketch that proves the termination of crack propagation. First, we assume that the integral in Eqn.2.2.2 is essentially constant when the crack is sufficiently long (it should recover the stress intensity factor for a penny-shaped crack). Taking derivative with respect to the crack length L, we have

$$\frac{\partial K_{Ic}}{\partial L} \propto \frac{\partial (p_p - \sigma_0)}{\partial L}\sqrt{L} + \frac{\partial \sqrt{L}}{\partial L}(p_p - \sigma_0) \tag{A.1}$$

Assuming the ideal gas law, we have

$$p_p V \approx const \tag{A.2}$$

$$p_p L^3 \approx const \tag{A.3}$$

$$\implies \frac{\partial (p_p - \sigma_0)}{\partial L} = \frac{\partial p_p}{\partial L} = -\frac{const}{L^4}. \tag{A.4}$$

Plugging Eqn.A.4 into Eqn.A.1, we have

$$\begin{aligned}\frac{\partial K_{Ic}}{\partial L} &\propto -\frac{A}{L^4}\sqrt{L} + \frac{B}{\sqrt{L}}(p_p - \sigma_0) \\ &= \frac{1}{\sqrt{L}}\left(Bp_p - B\sigma_0 - \frac{A}{L^3}\right) \\ &= \frac{1}{\sqrt{L}}\left(\frac{C}{L^3} - B\sigma_0 - \frac{A}{L^3}\right) \\ &= \frac{1}{\sqrt{L}}\left(\frac{D}{L^3} - B\sigma_0\right)\end{aligned}$$

for some constants A, B, C and D. When $L \to \infty$, $D/L^3 \to 0$, and

$$\frac{\partial K_{Ic}}{\partial L} \to -\frac{B}{\sqrt{L}}\sigma_0 < 0,$$

which implies that the stress intensity factor will eventually drop below the fracture toughness, ensuring the stability of the crack propatation.

Bibliography

[1] Mustafa Al Ibrahim and Tapan Mukerji. Thermal maturation effects on the elastic properties of organic-rich mudrocks. In *SEG Technical Program Expanded Abstracts 2017*, pages 3955–3960. Society of Exploration Geophysicists, 2017.

[2] Yazeed Alaudah and Ghassan AlRegib. A weakly supervised approach to seismic structure labeling. In *SEG Technical Program Expanded Abstracts 2017*, pages 2158–2163. Society of Exploration Geophysicists, 2017.

[3] Yazeed Alaudah, Shan Gao, and Ghassan AlRegib. Learning to label seismic structures with deconvolution networks and weak labels. In *SEG Technical Program Expanded Abstracts 2018*, pages 2121–2125. Society of Exploration Geophysicists, 2018.

[4] Adam M Allan, Anthony C Clark, Tiziana Vanorio, Waruntorn Kanitpanyacharoen, and Hans-Rudolf Wenk. On the evolution of the elastic properties of organic-rich shale upon pyrolysis-induced thermal maturation. *Geophysics*, 81(3):D263–D281, 2016.

[5] Adam M. Allan, Anthony C. Clark, Tiziana Vanorio, Waruntorn Kanitpanyacharoen, and Hans-Rudolf Wenk. On the evolution of the elastic properties of organic-rich shale upon pyrolysis-induced thermal maturation. *GEOPHYSICS*, 81(3):D263–D281, 2016.

[6] Mauricio Araya-Polo, Taylor Dahlke, Charlie Frogner, Chiyuan Zhang, Tomaso Poggio, and Detlef Hohl. Automated fault detection without seismic processing. *The Leading Edge*, 36(3):208–214, 2017.

[7] Barry Kean Atkinson. Subcritical crack growth in geological materials. *Journal of Geophysical Research: Solid Earth*, 89(B6):4077–4114, 1984.

[8] George E Backus. Long-wave elastic anisotropy produced by horizontal layering. *Journal of Geophysical Research*, 67(11):4427–4440, 1962.

[9] Kaushik Bandyopadhyay. *Seismic anisotropy: Geological causes and its implications to reservoir geophysics*. Stanford University, 2009.

[10] Michael Batzle and Zhijing Wang. Seismic properties of pore fluids. *Geophysics*, 57(11):1396, 1992.

[11] Robert R Berg and Anthony F Gangi. Primary migration by oil-generation microfracturing in low-permeability source rocks: application to the austin chalk, texas. *AAPG bulletin*, 83(5):727–756, 1999.

[12] Alan K Burnham. A simple kinetic model of oil generation, vaporization, coking, and cracking. *Energy & Fuels*, 29(11):7156–7167, 2015.

[13] Alan K Burnham and Robert L Braun. Development of a detailed model of petroleum formation, destruction, and expulsion from lacustrine and marine source rocks. *Organic Geochemistry*, 16(1-3):27–39, 1990.

[14] RM Capuano. Evidence of fluid flow in microfractures in geopressured shales. *AAPG Bulletin*, 77(8):1303–1314, 1993.

[15] José M Carcione and Per Avseth. Rock-physics templates for clay-rich source rocks. *Geophysics*, 80(5):D481–D500, 2015.

[16] José M Carcione, Hans B Helle, and Per Avseth. Source-rock seismic-velocity models: Gassmann versus backus. *Geophysics*, 76(5):N37–N45, 2011.

[17] Michael R Chandler, Philip G Meredith, Nicolas Brantut, and Brian R Crawford. Fracture toughness anisotropy in shale. *Journal of Geophysical Research: Solid Earth*, 121(3):1706–1729, 2016.

[18] KP Chong, K Uenishi, JW Smith, and AC Munari. Non-linear three dimensional mechanical characterization of colorado oil shale. In *International Journal of Rock Mechanics and Mining Sciences & Geomechanics Abstracts*, volume 17, pages 339–347. Elsevier, 1980.

[19] Radim Ciz and Serge A Shapiro. Generalization of gassmann equations for porous media saturated with a solid material. *Geophysics*, 72(6):A75–A79, 2007.

[20] PJ Closmann and WB Bradley. The effect of temperature on tensile and compressive strengths and young's modulus of oil shale. *Society of Petroleum Engineers Journal*, 19(05):301–312, 1979.

[21] Olivier Coussy, L Dormieux, and F Schneider. A mechanical modelling of the primary migration. *Revue de l'Institut Francais du Petrole*, 53(2):151–162, 1998.

[22] Mark E Curtis, Carl H Sondergeld, and Chandra S Rai. Investigation of the microstructure of shales in the oil window. In *Unconventional Resources Technology Conference*, pages 1597–1602. Society of Exploration Geophysicists, American Association of Petroleum Geologists, Society of Petroleum Engineers, 2013.

[23] Vishal Das, Ahinoam Pollack, Uri Wollner, and Tapan Mukerji. Convolutional neural network for seismic impedance inversion. In *SEG Technical Program Expanded Abstracts 2018*, pages 2071–2075. Society of Exploration Geophysicists, 2018.

[24] dGB Earth Sciences B.V. Netherlands offshore f3 block, 1987. `https://www.opendtect.org/osr/Main/NetherlandsOffshoreF3BlockComplete4GB`.

[25] R Di Primio and B Horsfield. From petroleum-type organofacies to hydrocarbon phase prediction. *AAPG bulletin*, 90(7):1031–1058, 2006.

[26] Simon Emmanuel, Moshe Eliyahu, Ruarri J Day-Stirrat, Ronny Hofmann, and Calum I Macaulay. Softening of organic matter in shales at reservoir temperatures. *Petroleum Geoscience*, 23(2):262–269, 2017.

[27] E Eseme, JL Urai, BM Krooss, and R Littke. Review of mechanical properties of oil shales: Implications for exploitation and basin modelling. *Oil Shale*, 24(2):159–175, 2007.

[28] ZQ Fan, Z-H Jin, and SE Johnson. Subcritical propagation of an oil-filled penny-shaped crack during kerogen–oil conversion. *Geophysical Journal International*, 182(3):1141–1147, 2010.

[29] ZQ Fan, Z-H Jin, and SE Johnson. Modelling petroleum migration through microcrack propagation in transversely isotropic source rocks. *Geophysical Journal International*, 190(1):179–187, 2012.

[30] JC Goff. Hydrocarbon generation and migration from jurassic source rocks in the e shetland basin and viking graben of the northern north sea. *Journal of the Geological Society*, 140(3):445–474, 1983.

[31] Ian Goodfellow, Jean Pouget-Abadie, Mehdi Mirza, Bing Xu, David Warde-Farley, Sherjil Ozair, Aaron Courville, and Yoshua Bengio. Generative adversarial nets. In Z. Ghahramani, M. Welling, C. Cortes, N. D. Lawrence, and K. Q. Weinberger, editors, *Advances in Neural Information Processing Systems 27*, pages 2672–2680. Curran Associates, Inc., 2014.

[32] Brian E. Hornby, Larry M. Schwartz, and John A. Hudson. Anisotropic effectivemedium modeling of the elastic properties of shales. *GEOPHYSICS*, 59(10):1570–1583, 1994.

[33] Lei Huang, Xishuang Dong, and T Edward Clee. A scalable deep learning platform for identifying geologic features from seismic attributes. *The Leading Edge*, 36(3):249–256, 2017.

[34] Charles Rutherford Ildstad and Peter Bormann. Using 3d segy seismic and 3d convolutional neural networks to map and classify seismic facies. `https://github.com/bolgebrygg/MalenoV`, 2017.

[35] John Conrad Jaeger, Neville GW Cook, and Robert Zimmerman. *Fundamentals of rock mechanics*. John Wiley & Sons, 2009.

[36] Morten Jakobsen, John A Hudson, Tim A Minshull, and Satish C Singh. Elastic properties of hydrate-bearing sediments using effective medium theory. *Journal of Geophysical Research: Solid Earth*, 105(B1):561–577, 2000.

[37] Daniel M Jarvie. Total organic carbon (toc) analysis: Chapter 11: geochemical methods and exploration. 1991.

[38] Z-H Jin, Scott E Johnson, and ZQ Fan. Subcritical propagation and coalescence of oil-filled cracks: Getting the oil out of low-permeability source rocks. *Geophysical Research Letters*, 37(1), 2010.

[39] Leonie E. A. Jones and Herbert F. Wang. Ultrasonic velocities in cretaceous shales from the williston basin. *GEOPHYSICS*, 46(3):288–297, 1981.

[40] Barry Katz. *Petroleum source rocks*. Springer Science & Business Media, 2012.

[41] Diederik P. Kingma and Jimmy Ba. Adam: A method for stochastic optimization, 2014.

[42] Maya Kobchenko, Hamed Panahi, Francois Renard, Dag K Dysthe, Anders Malthe-Sørenssen, Adriano Mazzini, Julien Scheibert, Bjørn Jamtveit, and Paul Meakin. 4d imaging of fracturing in organic-rich shales during heating. *Journal of Geophysical Research: Solid Earth*, 116(B12), 2011.

[43] Vikas Kumar, Mark Erman Curtis, Nabanita Gupta, Carl H Sondergeld, Chandra Shekhar Rai, et al. Estimation of elastic properties of organic matter in woodford shale through nanoindentation measurements. In *SPE Canadian Unconventional Resources Conference*. Society of Petroleum Engineers, 2012.

[44] Guy T Kuster and M Nafi Toksöz. Velocity and attenuation of seismic waves in two-phase media: Part i. theoretical formulations. *Geophysics*, 39(5):587–606, 1974.

[45] KY Lam and SP Phua. Multiple crack interaction and its effect on stress intensity factor. *Engineering Fracture Mechanics*, 40(3):585–592, 1991.

[46] Gary G Lash and Terry Engelder. An analysis of horizontal microcracking during catagenesis: Example from the catskill delta complex. *AAPG bulletin*, 89(11):1433–1449, 2005.

[47] Yann LeCun, Léon Bottou, Yoshua Bengio, and Patrick Haffner. Gradient-based learning applied to document recognition. *Proceedings of the IEEE*, 86(11):2278–2324, 1998.

[48] M. D. Lewan, J. C. Winters, and J. H. McDonald. Generation of oil-like pyrolyzates from organic-rich shales. *Science*, 203(4383):897–899, 1979.

[49] MD Lewan. Laboratory simulation of petroleum formation. In *Organic geochemistry*, pages 419–442. Springer, 1993.

[50] Michael D Lewan and Allison A Henry. *Gas: oil ratios for source rocks containing Type-I,-II,-IIS, and-III kerogens as determined by hydrous pyrolysis*. US Department of the Interior, US Geological Survey, 1999.

[51] Jonathan Long, Evan Shelhamer, and Trevor Darrell. Fully convolutional networks for semantic segmentation. In *Proceedings of the IEEE conference on computer vision and pattern recognition*, pages 3431–3440, 2015.

[52] Robert G Loucks, Robert M Reed, Stephen C Ruppel, and Daniel M Jarvie. Morphology, genesis, and distribution of nanometer-scale pores in siliceous mudstones of the mississippian barnett shale. *Journal of sedimentary research*, 79(12):848–861, 2009.

[53] Xiaorong Luo and Guy Vasseur. Geopressuring mechanism of organic matter cracking: numerical modeling. *AAPG bulletin*, 80(6):856–873, 1996.

[54] Gary Mavko, Tapan Mukerji, and Jack Dvorkin. *The rock physics handbook: Tools for seismic analysis of porous media*. Cambridge university press, 2009.

[55] Gary Mavko and Nishank Saxena. Rock-physics models for heterogeneous creeping rocks and viscous fluids. *GEOPHYSICS*, 81(4):D427–D440, 2016.

[56] Lukas Mosser, Olivier Dubrule, and Martin J. Blunt. Reconstruction of three-dimensional porous media using generative adversarial neural networks. *Phys. Rev. E*, 96:043309, Oct 2017.

[57] MJP Musgrave. *Crystal acoustics*. Acoustical Society of America New York, 2003.

[58] RH Nilson and WJ Proffer. Engineering formulas for fractures emanating from cylindrical and spherical holes. *Journal of applied mechanics*, 51(4):929–933, 1984.

[59] Osamu Nishizawa. Seismic velocity anisotropy in a medium containing oriented cracks. *Journal of Physics of the Earth*, 30(4):331–347, 1982.

[60] Audrey Ougier-Simonin, François Renard, Claudine Boehm, and Sandrine Vidal-Gilbert. Microfracturing and microporosity in shales. *Earth-Science Reviews*, 162:198–226, 2016.

[61] Ismail Özkaya. A simple analysis of oil-induced fracturing in sedimentary rocks. *Marine and Petroleum Geology*, 5(3):293–297, 1988.

[62] KE Peters, AK Burnham, and CC Walters. Petroleum generation kinetics: Single versus multiple heating-ramp open-system pyrolysis: Reply. *AAPG Bulletin*, 100(4):690–694, 2016.

[63] Kenneth E Peters and Mary Rose Cassa. Applied source rock geochemistry: Chapter 5: Part ii. essential elements. 1994.

[64] A Pimmel and G Claypool. Introduction to shipboard organic geochemistry on the joides resolution. 2001.

[65] Xuan Qin, De-hua Han, and Luanxiao Zhao. Rock physics modeling of organic-rich shales with different maturity levels. In *SEG Technical Program Expanded Abstracts 2014*, pages 2952–2957. Society of Exploration Geophysicists, 2014.

[66] Olaf Ronneberger, Philipp Fischer, and Thomas Brox. U-net: Convolutional networks for biomedical image segmentation. In *International Conference on Medical image computing and computer-assisted intervention*, pages 234–241. Springer, 2015.

[67] Colin M. Sayers. The effect of kerogen on the elastic anisotropy of organic-rich shales. *GEOPHYSICS*, 78(2):D65–D74, 2013.

[68] Richard C Selley and Stephen A Sonnenberg. *Elements of petroleum geology*. Academic Press, 2014.

[69] Igor Sevostianov, Nadir Yilmaz, Vladimir Kushch, and Valery Levin. Effective elastic properties of matrix composites with transversely-isotropic phases. *International Journal of Solids and Structures*, 42(2):455 – 476, 2005. Micromechanics of Materials.

[70] André LD Spigolon, Michael D Lewan, Henrique L de Barros Penteado, Luiz Felipe C Coutinho, and João G Mendonça Filho. Evaluation of the petroleum composition and quality with increasing thermal maturity as simulated by hydrous pyrolysis: A case study using a brazilian source rock with type i kerogen. *Organic Geochemistry*, 83:27–53, 2015.

[71] ND Stout, GJ Koskinas, JH Raley, SD Santor, RJ Opila, and AJ Rothman. Pyrolysis of oil shale: the effects of thermal history on oil yield. Technical report, California Univ., Livermore (USA). Lawrence Livermore Lab., 1976.

[72] Jerry J Sweeney and Alan K Burnham. Evaluation of a simple model of vitrinite reflectance based on chemical kinetics (1). *AAPG bulletin*, 74(10):1559–1570, 1990.

[73] Leon Thomsen. Weak elastic anisotropy. *Geophysics*, 51(10):1954–1966, 1986.

[74] Chuan Tian. *Machine Learning Approaches for Permanent Downhole Gauge Data Interpretation*. PhD thesis, Stanford University, 2018.

[75] Chuan Tian and Roland Horne. Applying machine-learning techniques to interpret flow-rate, pressure, and temperature data from permanent downhole gauges. *SPE Reservoir Evaluation & Engineering*, 2019.

[76] BP Tissot and DH Welte. Petroleum formation and occurrence-a new approach to oil and gas exploration, 1984.

[77] Ilya Tsvankin. *Seismic signatures and analysis of reflection data in anisotropic media*. Society of Exploration Geophysicists, 2012.

[78] Lev Vernik. Hydrocarbon-generation-induced microcracking of source rocks. *Geophysics*, 59(4):555–563, 1994.

[79] AU Waldeland and AHSS Solberg. Salt classification using deep learning. In *79th EAGE Conference and Exhibition*, 2017.

[80] Wenlong Wang, Fangshu Yang, and Jianwei Ma. Velocity model building with a modified fully convolutional network. In *SEG Technical Program Expanded Abstracts 2018*, pages 2086–2090. Society of Exploration Geophysicists, 2018.

[81] Yunfei Yang and Gary Mavko. Hydrous pyrolysis-based rock-physics modeling for organic-rich shales at various levels of thermal maturity. In *SEG Technical Program Expanded Abstracts 2018*, pages 3744–3748. Society of Exploration Geophysicists, 2018.

[82] Yunfei Yang and Gary Mavko. Mathematical modeling of microcrack growth in source rock during kerogen thermal maturation. *AAPG Bulletin*, (20,180,604), 2018.

[83] Saeed Zargari, Manika Prasad, Kenechukwu C Mba, and Earl D Mattson. Organic maturity, elastic properties, and textural characteristics of self resourcing reservoirs. *Geophysics*, 78(4):D223–D235, 2013.

[84] Jonathan C Zeszotarski, Richard R Chromik, Richard P Vinci, Marie C Messmer, Raymond Michels, and John W Larsen. Imaging and mechanical property measurements of kerogen via nanoindentation. *Geochimica et cosmochimica acta*, 68(20):4113–4119, 2004.

[85] Feng Zhang, Xiang-yang Li, and Keran Qian. Estimation of anisotropy parameters for shale based on an improved rock physics model, part 1: theory. *Journal of Geophysics and Engineering*, 14(1):143, 2016.

[86] Luanxiao Zhao, Xuan Qin, De-Hua Han, Jianhua Geng, Zhifang Yang, and Hong Cao. Rock-physics modeling for the elastic properties of organic shale at different maturity stages. *Geophysics*, 81(5):D527–D541, 2016.